Journal of Molecular Liquids 407 (2024) 125262

Contents lists available at ScienceDirect

Journal of Molecular Liquids

journal homepage: www.elsevier.com/locate/molliq

Surface tension measurement and molecular simulation for new low global warming potential refrigerants R1132(E) and R1132a

Tomoaki Imai [a], Takemasa Kawahara [a], Ryutaro Nonaka [a], Sebastiano Tomassetti [b], Tetsuya Okumura [a], Yukihiro Higashi [c], Giovanni Di Nicola [b], Chieko Kondou [a,*]

[a] School of Engineering, Nagasaki University, Nagasaki 8528521, Japan
[b] Dipartimento di Ingegneria Industriale e Scienze Matematiche, Università Politecnica delle Marche, via Brecce Bianche 12, 60131 Ancona, Italy
[c] Research Center for Next Generation Refrigerant Properties (NEXT-RP), International Institute for Carbon-Neutral Energy Research (WPI-I2CNER), Kyushu University, 744 Motooka, Nishi-ku, Fukuoka 8190395, Japan

ARTICLE INFO

Keywords:
Surface tension
Low GWP refrigerants
Molecular dynamic simulation
Quantum chemical simulation
Parachor

ABSTRACT

This study performed surface tension measurements assisted by molecular simulations for new candidate refrigerants R1132(E) and its isomer R1132a, which exhibit extremely low global warming potentials. Because the measured saturation density required for the surface tension measurement by the differential capillary rise method is insufficient at low temperatures, the density data was extrapolated by molecular simulations. In the process, quantum chemical and molecular dynamics simulations were performed to reproduce the vapor–liquid equilibrium state, and the accuracy of the obtained molecular force fields was verified by comparing them with the measured data. Based on the obtained surface tension data, validated temperature correlation equations were proposed for R1132(E) and R1132a, respectively, validated in the temperature range from 209 K to 225 K. Furthermore, their parachors, which relate surface tension to saturation density, were determined from the above data as 116.1 and 116.7 for R1132(E) and R1132a, respectively.

1. Introduction

Global warming is recognized as an anthropogenic effect in IPCC AR6 [1], and the global crisis associated with a global average temperature increase of 1.5 to 2 K is now being analyzed. In addition to the climate crisis, global warming has complex and far-reaching effects such as ocean acidification, excessive use of nitrogen and phosphorus (fertilizers) due to the food crisis [2], and social instability due to mass migration resulting from the deterioration of living conditions [3]. The reduction of long-lived greenhouse gases, as well as CO_2, which accounts for the majority of greenhouse gas emissions, is important to minimize greenhouse gas emissions. Refrigerants have the longest atmospheric lifetimes. Hence, refrigeration and air-conditioning industries need to urgently switch to refrigerants with low global warming potentials (GWPs) [4]. However, no ideal refrigerant has been found that simultaneously satisfies the required criteria such as high energy efficiency, negligible acute toxicity, low flammability, and absence of polymerizations hazard (e.g., disproportionate reaction), although hydrofluoroolefins (HFOs) are attracting attention as a substance group with extremely low GWP [5]. In addition, some refrigerants contain water-soluble carcinogens generated during their decomposition. Consequently, many of these refrigerants have been eliminated as potential candidates for classification as controlled substances under the per- and poly fluoroalkyl substance (PFAS) environmental pollutant regulation [6]. Ethylene-derived HFO-based substances are among the few candidates suitable for such scenarios.

Table 1 summarizes the basic information regarding the substances R1132(E) and R1132a covered in this study. Both are ethylene fluorides with the molecular formula $C_2H_2F_2$; however, R1132(E) is the *trans*-form HFC = CFH, and R1132a is the structural isomer $CF_2 = CH_2$. The thermodynamic properties of the two materials, including their critical parameters, have been reported in several studies. The critical temperature of R1132a is 302.62 K [7], which is significantly lower than that of R1132(E) (348.82 K) [8]. The triple-point temperatures of R1132a and R1132(E) are notably disparate, at 111 K and 185 K [9], respectively, indicating a significant difference. Based on these data, R1132a and R1132(E) are the anticipated to be utilized as components in refrigerant mixtures for ultralow-temperature and air-conditioning equipment, respectively. However, information on their physical properties is insufficient for equipment design. For example, the surface tension required for accurate heat transfer coefficient calculations has not yet

* Corresponding author.
E-mail address: ckondou@nagasaki-u.ac.jp (C. Kondou).

https://doi.org/10.1016/j.molliq.2024.125262
Received 15 February 2024; Received in revised form 17 May 2024; Accepted 11 June 2024
Available online 15 June 2024
0167-7322/© 2024 The Author(s). Published by Elsevier B.V. This is an open access article under the CC BY-NC-ND license (http://creativecommons.org/licenses/by-nc-nd/4.0/).

Nomenclature

a^2	capillary constant [m^2]
D	half of interfacial thickness [m]
g	local gravitational acceleration [m s^{-2}]
g_n	normal gravitational acceleration (=9.80665 ms^{-2})[m s^{-2}]
Δh_c	corrected differential capillary rise height[m]
Δh_m	measured differential capillary rise height[m]
k_B	Boltzmann constant (=1.380649 × 10^{-23} J K^{-1}) [J K^{-1}]
k_r	force constant of bonding [J mol^{-1} m^{-2}]
k_θ	force constant of angle [J mol^{-1} rad^{-2}]
k_ϕ	force constant of dihedral [J mol^{-1}]
Lz	length of simulation cell box in the z-direction [m]
MM	molar mass [kg mol^{-1}]
n	constant in Eq. (1) [-]
P	pressure or pressure tensor [Pa]
$[P]$	parachor parameter [$(mNm^{-1})^{1/4}cm^3mol^{-1}$]
q	partial charge [C]
r	bond length or capillary radius [m]
r_0	bond length of equilibrium [m]
r_{ij}	distance between two non-bonded atoms i and j[m]
T	temperature [K]
T_R	reduced temperature (=T/T_{crit}) [-]
U_{bonded}	bonding energy [J mol^{-1}]
$U_{non\text{-}bonded}$	nonbonding energy [J mol^{-1}]
z	position in z direction [m]
z_R	position of interface at right [m]
z_L	position of interface at left [m]

Greek symbols

γ	surface tension [N m^{-1}]
ε_0	vacuum permittivity [F m^{-1}]
ε	Lenard-Jones potential energy[J mol^{-1}]
ϕ	dihedral angle[rad]
ϕ_0	phase angle[rad]
θ	angle[rad]
θ_0	equilibrium angle[rad]
ν	molar volume [m^3 mol^{-1}]
ρ	density [kg m^{-3}]
ρ'	liquid density [kg m^{-3}]
ρ''	vapor density [kg m^{-3}]
$\tilde{\rho}'$	molar liquid density [mol m^{-3}]
$\tilde{\rho}''$	molar vapor density[mol m^{-3}]
σ	Lenard-Jones potential collision diameter [m]
φ	contact angle [rad]
ω	acentric factor [-]

Subscripts

crit	critical point
empirical	empirical correlation
HT	Hankinson-Thomson correlation
sat	saturated
x	x direction
y	y direction
z	z direction

Table 1
Basic information of the target substances, R1132(E) and R1132a.

ASHRAE refrigerant number [a]	R1132(E)	R1132a
IUPAC chemical name	*trans*-1,2-difluoroethylene	1,1-difluoroethene
CAS no.	1630–78-0	75–38-7
Molar mass [g mol^{-1}]	64.035	64.035
Critical temperature [K]	348.82 ± 0.01[b]	302.62 ± 0.01 [e]
Critical pressure [kPa]	5172.5 ± 1.0[c]	4448.0 ± 2.0 [e]
Critical density [kg m^{-3}]	438 ± 5[b]	414 ± 5 [e]
Acentric factor	0.2433[c, f]	0.176 [e, f]
Triple point temperature [K]	184.9 [d]	111.0 [d]

[a]ASHRAE [19], [b]Sakoda et al. [8], [c]Perera et al. [20], [d]Tomassetti et al. [9], [e]Perera et al. [7].
[f] defined by the saturation pressure at the converted temperature of 0.7, $\omega = -\log_{10}(P_{sat})_{T_r=0.7} - 1$ [21].

Table 2
Selected methods and options in MO and MD simulations. *.

	MO
Software	Gaussian 16 W [27]
Optimization	CCSD/DGTZVP [39–41] "geom = connectivity, scf = tight" **
Energy	CCSD/DGTZVP"iop (6/41 = 10,6/42 = 17,6/50 = 1), scf = tight" **
Charge assignment scheme	RESP [23] assigned by Antechamber [28,29]
Scanning	CCSD/DGTZVP "opt = modredundant, geom = connectivity, scf = tight"
	MD
Code	GROMACS 2016 double precision [42]
Number of molecules	2500 ~ 3000
Boundary	Periodic in x, y, and z directions
Integrator	Leap-flog [43,44]
Ensemble	NVT
Velocity generation	Maxwell distribution with random seed with NVT ensemble
Time step	0.5 fs
Equilibration period	4 – 10 ns
Sampling period	2 – 3 ns
vdW cutoff	1.5 nm
Coulomb	Particle-mesh Ewald [45]
Coulomb cutoff	1.5 nm
Temperature coupling	Nose-Hoover chain [46,47]
Holonomic constraints	Hydrogen bonding (w/o angle constraint) using LINCS algorithm [48]

* The used mol2 files and Gromacs topology files are included in the Appendix.
** The descriptions in quotation marks "" indicate the input file entries.

been reported with a high accuracy.

Raabe et al. successfully used molecular simulation, specifically Gibbs ensemble Monte Carlo (GEMC) simulation, to quantitatively predict the vapor–liquid saturation densities and saturation pressures of several propylene-based HFO substances, whose measurements were insufficient [10–14]. These methods can also be applied to molecular dynamics (MD) simulations to predict the saturation densities of the ethylene-based target substances, R1132(E) and R1132a. This study calculated the vapor–liquid coexistence curves and saturation pressures from near the triple point to the critical point, using molecular simulations and verified them against experimental data. Furthermore, the surface tension was measured from 235 K to 300 K using the data obtained from vapor-liquid coexistence curves. On the other hand, research using MD simulations for surface tension is also progressing. Recent trends in the past approximately 15 years include studies focusing on the unique surface activity induced at the vapor–liquid interface of binary mixtures [15–18]. In this study, MD simulations were also used to predict surface tension at low temperatures, where measurement is difficult.

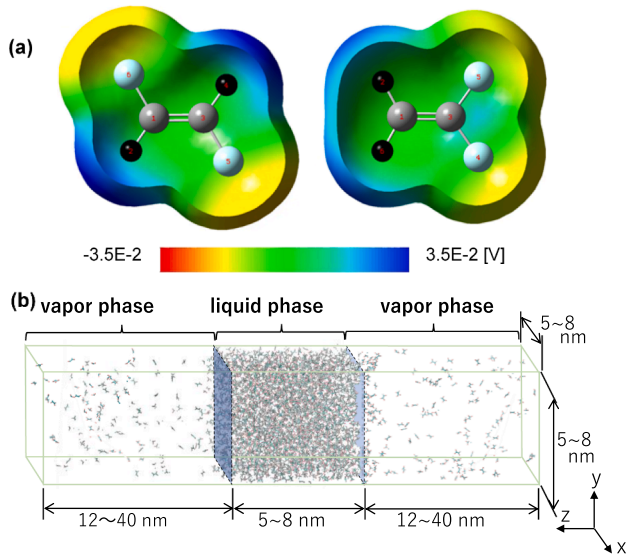

Fig. 1. Simulation model. (a) Electrostatic potential mapped on an *iso*-electron-density surface of 0.0004*e* Å^{-3}. The contour represents the electro static potential energy in Volts. The force field used in MD was built from the MO results. (b) Cell box for vapor–liquid equilibrium used in the MD simulation. Periodic boundary conditions were applied to all surfaces. Under zero gravity conditions, a thin liquid film, surrounded by saturated vapor, exists in the center.

2. Simulation

The following procedure was employed to simulate a vapor–liquid equilibrium system to obtain density values at low temperatures, where experimental data was insufficient. First, molecular orbital (MO) simulations were performed to develop molecular force fields for R1132(E) and R1132a. The MD simulation reproduced a vapor–liquid equilibrium system of 2,000–3,000 molecules using a molecular force field of the all-atom model. Since the target substance has only six constituent atoms, the rigid model could be advantageous in reducing computational cost. Subsequently, physical properties, such as orthobaric density, were computed by a statistical treatment. Table 2 lists the methods and options used in these simulations. The following provides a detailed description of the techniques used in the MO and MD simulations.

The bonded interaction used in this study consists of harmonic bond stretching and harmonic angle-vibration potentials, and period-type proper dihedral potentials can be expressed as

$$U_{\text{bonded}} = \sum \frac{1}{2}k_r(r - r_0)^2 + \sum \frac{1}{2}k_\theta(\theta - \theta_0)^2 + \sum k_\phi[1 + \cos(n\phi - \phi_0)] \quad (1)$$

The bonded interaction is parameterized by the equilibration bonding length and angle, as well as the spring constants k_r (kJ mol^{-1} nm^{-2}) and k_θ (kJ mol^{-1} rad^{-2}), obtained by MO simulation. The third term ϕ denotes the dihedral angle. The phase angle ϕ_0 takes the values of either 0° or 180°. Because the two target substances are ethylene derivatives and are tightly bonded at a dihedral angle of 180° with a carbon–carbon double bond as the backbone, the dihedral angle parameters of AMBER03 [22] were adopted.

The nonbonded interaction in this study consists of Coulomb and van der Waals forces, formulated by the following equation. The 12–6 Lennard–Jones interaction form was employed as the van der Waals term.

$$U_{\text{non - bonded}} = \sum \frac{q_i q_j}{4\pi\varepsilon_0 r_{ij}} + \sum 4\varepsilon_{ij}\left[\left(\frac{\sigma_{ij}}{r_{ij}}\right)^{12} - \left(\frac{\sigma_{ij}}{r_{ij}}\right)^{6}\right] \quad (2)$$

These two interactions between atoms separated by three covalent bonds (e.g., 1–4 interactions) were considered by multiplying the scaling factor by 0.5. The partial static charges q at the atomic nuclei were assigned from the MO simulation, using the restrained electrostatic potential (RESP) scheme [23]. The Lennard–Jones parameters ε and σ, which are based on those proposed by Raabe for R1123 and R1234yf, are fine-tuned to be consistent with the saturation density measured near the critical point. σ was adjusted primarily to match the saturated liquid density at lower temperatures, while ε was adjusted to reproduce the density curve asymptotically toward the critical temperature. These adjustments were done through trial and error, with a cutoff of 1.5 nm, and based on density measurement data, ensuring no significant deviation from values given by OPLS-AA/L[24], Raabe's works[25,26], and AMBER03[22]. For heteroatomic combinations, ε and σ were calculated using the Lorentz–Berthelot rule:

$$\varepsilon_{ij} = \sqrt{\varepsilon_{ii} + \varepsilon_{jj}} \text{ and } \sigma_{ij} = \frac{\sigma_{ii} + \sigma_{jj}}{2} \quad (3)$$

The structures of the R1132(E) and R1132a monomers were optimized using the CCSD/DGTZVP basis sets of Gaussian16W [27]. Energy calculations associated with the options listed in Table 2 were performed to obtain partial charges, which are a portion of the molecular force field. The contour in Fig. 1 (a) represents the electrostatic potential energy in Volts (V), mapped on an *iso*-electron-density surface of 0.0004*e* Å^{-3}. Based on the results obtained, a RESP [23] was assigned using the Antechamber program [28,29]. Scanning calculations were performed to obtain bond and angle spring coefficients, indicating the intramolecular potentials. The molecular force field was constructed by adding the Lennard–Jones parameters, assigned by the general force field OPLS-AA/L [24], to the obtained values. Although various other general force fields have been developed (e.g., CGENFF [30], COMPASS III [31], CVFF [32], DREIDING-UT [33]) corresponds to the classical potential formula of the all-atom model, the OPLS-AA/L developed for small molecule solutions was employed in this study.

Fig. 1(b) shows the vapor–liquid equilibrium model used in the MD simulations, reproduced in a cell box with periodic boundary conditions. The model simulates the existence of a thin liquid film that extends infinitely into the *x*-*y* plane in a vapor-filled volume, under zero-gravity. The number of molecules was set to 2500–3000 and equilibrated for 4–10 ns using an NVT ensemble. At low temperatures, the vapor space widens when the number of molecules in the vapor phase is negligible. Cutoff values and other conditions are listed in Table 2. The saturation density, saturation pressure, etc., were calculated from the molecular distribution and normal pressure obtained by MD, as follows.

The bulk saturated liquid density (ρ') and saturated vapor density (ρ'') were calculated by fitting the *z*-directional density distribution $\rho(z)$ averaged over 1–2 ns using the following equation [34]:

$$\rho(z) = \rho'' + \frac{\rho' - \rho''}{2}\left\{\tanh\frac{z - z_R}{D} - \tanh\frac{z - z_L}{D}\right\} \quad (4)$$

where z_L and z_R indicate the positions of the vapor–liquid interface on the left and right sides, respectively. D represents half of the interface thickness. The saturation pressure corresponds to the normal pressure tensor in the *z*-direction perpendicular to the vapor–liquid interface, averaged over the entire box cell and further averaged over the sampling time, $\langle P_{zz}\rangle$. Surface tension (γ) can also be obtained as follows.

$$\gamma = \left[\langle P_{zz}\rangle - \frac{\langle P_{xx}\rangle + \langle P_{yy}\rangle}{2}\right]\frac{L_z}{2} \quad (5)$$

The tail collection effect [35], which considers the effect beyond the cutoff radius, is reported to be negligibly small by a factor of 4 to 5 or more for the Lennard–Jones parameter, σ [36,37]. This factor ranges from 4.16 to 6.12 in the present simulation; thus, the effect of tail correction can be considered negligible. This influence is discussed in more detail in Section 4. The NP$_{zz}$AT ensemble has been demonstrated to be effective in improving the accuracy of surface tension calculations [38]. However, complete equilibration could not be achieved owing to

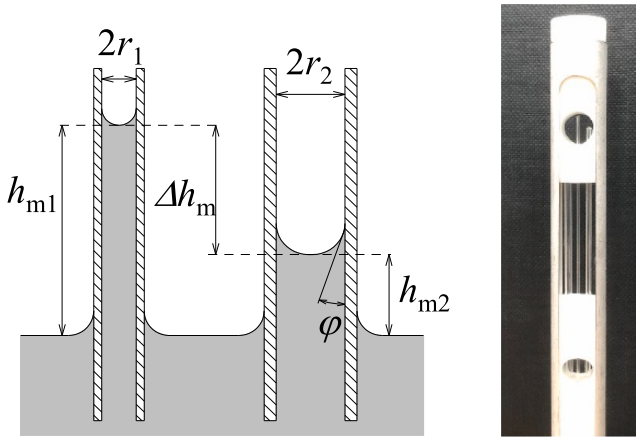

Fig. 2. Principle of the measurement method (left) and tested capillary tubes (right). Glass capillaries with inner radii of 0.7234 ± 0.002 mm, 0.4021 ± 0.002 mm, and 0.2513 ± 0.002 mm were used in this study. The three capillaries were held vertically using two silicon grippers.

the high volatility of the substances addressed in this study.

3. Measurement

Fig. 2 shows the principle of the differential capillary rise method for measuring surface tension and a photograph of the glass capillaries and supporting brace used in the experiment. In a capillary with its lower end immersed in a liquid, the liquid rises with surface tension, and the height of the liquid column is determined by the balance between the surface tension and body force acting in the direction of gravity. By measuring the difference in height between the two liquid columns at the bottom of the meniscus and approximating the meniscus as a hemisphere, the height can be modified as follows [49]

$$\Delta h_c \approx \Delta h_m + \frac{(r_1 - r_2)}{3} \tag{6}$$

The capillary constant a^2 was obtained from the corrected differential capillary height (Δh_c), using the following equation:

$$a^2 = \frac{g\Delta h_c}{g_n(1/r_1 - 1/r_2)cos\varphi} \approx \frac{g\Delta h_c}{g_n(1/r_1 - 1/r_2)} \tag{7}$$

where g_n and g are the standard gravitational acceleration and gravitational acceleration at the measurement location, respectively.

$$\gamma = \frac{a^2 g_n(\rho' - \rho'')}{2} \tag{8}$$

where, ρ' and ρ'' denote the saturated liquid and vapor densities. The liquid density ρ' is given by the Hankinson–Thomson correlation [27] of the vapor–liquid coexistence curve, obtained based on the measurements and MD simulations. Meanwhile, the vapor density ρ'' is given by the Peng–Robinson equation of state. If an accurate saturation density is reported in the future, the capillary constant reported herein and new density data can be substituted into Eq. (8) to obtain the correct surface tension.

The difference in capillary rise between the two capillary tubes was measured using a digital traveling microscope with a 0.01 mm tolerance. Three glass capillaries with different inner radii were used, as shown in the photograph of Fig. 2, and the arithmetic mean of the obtained three capillary constants and surface tensions were determined as the measured value. The inner radii of the capillaries were measured with a mercury slug [50]. The mass and length of an injected mercury slag in the glass capillary were measured, and its radius was calculated, assuming that both ends of the mercury slag were hemispherical. The capillaries and sample refrigerant were set in a pressure vessel placed in a thermostatic chamber with a controllable fluctuation range of 10–223 K [51]. The temperature was measured with a 100 Ω platinum resistance thermometer calibrated against ITS-90. The uncertainty in the temperature measurement was estimated to be within 5 mK. An exception was made for the surface-tension measurement of R1132a, which was cooled using liquid nitrogen and aluminum beads to cool it to 209 K. The temperature control accuracy in this data series was 1 K, and the temperature variation around the pressure vessel was approximately 1 K. This resulted in significant measurement uncertainty. Nevertheless, the data in such a low temperature range is valuable and is therefore referenced in this study.

Table 3
Sample purity and vendor used in the present surface tension measurement.

ASHRAE refrigerant number [a]	R1132(E)	R1132a
Purity in moles	99.6–99.9 %	99.7 % (initial) final purity > 99.9 %
Vendor	Daikin Industries, Ltd.	

The purities of the samples are listed in Table 3. The initial purity of R1132a was relatively low at 99.7 % due to the presence of inert gas. After the R1132a samples were filled in a stainless-steel container, they were degassed with liquid nitrogen in repeated freeze–thaw cycles until the pressure was below 10^{-3} Pa in frozen state. After degassing, the purity was confirmed as 99.9 % or higher by thermal conductivity gas chromatography.

4. Simulation results

4.1. Bond stretching and angle vibration

Fig. 3 plots energy variation against bonding length and angle for the R1132(E) and R1132a monomers. The horizontal axes indicate the bond lengths or bond angles. Symbols were obtained by the MO simulation (scanning with CCSD/DGTZVP), instead of being assigned by a general force field AMBER03 [22], shown with dashed lines. The simulated equilibrium bonding lengths agreed with the AMBER03 within 0.005 nm; however, the equilibrium bonding angles deviated by approximately 5° in some cases. This difference appears to be mainly because of the steric hindrance of π-bonds. Accordingly, the parameters used in the MD simulation refer to these simulation results. Table 4 lists the adopted force filed parameters expressing bonded interaction. The energy calculated with the adopted parameters is plotted with solid lines in Fig. 3.

4.2. Coulomb and van der Waals interactions

Table 5 lists the non-bond interaction parameters that were finally determined. The partial charges were then assigned by the MO simulation and RESP scheme. LJ parameters were adjusted to match the measured saturated liquid density. The saturation pressure and vapor–liquid coexistence curve, obtained from MD simulation using these parameters, are shown in Fig. 5 and Fig. 6.

4.3. Saturation pressure and vapor–liquid coexistence curve

Fig. 4 plots the density distribution near the liquid film in the vapor–liquid equilibrium system simulated by MD. The symbols are the densities obtained by averaging the values of 50 to 100 slices of the simulation cell box in the z-direction over a time period of 2 to 3 ns after performing the equilibration. The density distributions averaged over the interval indicated by the symbols in Fig. 4 were approximately represented by Eq. (3) (shown with the lines). More detailed profile of the interfacial density at temperatures near the triple point would have revealed oscillatory layering near the vapor–liquid interface [52,53]. To

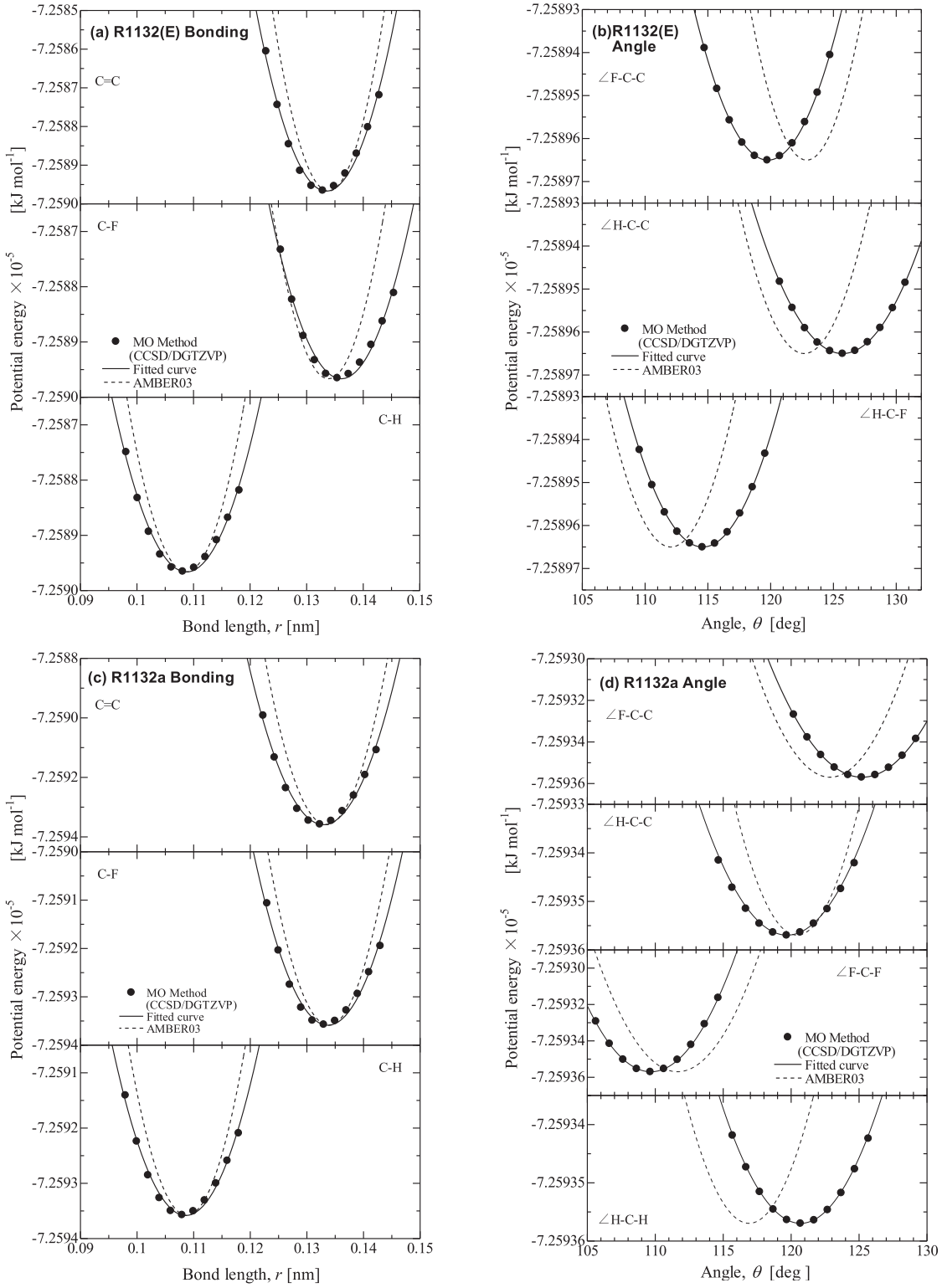

Fig. 3. Simulated energy variation against bond length and angle. (a) R1132(E) bonding, (b) R1132(E) angle, (c) R1132a bonding, and (d) R1132a angle. The horizontal axes indicate displacement, and the vertical axes indicate energy. The symbols are the MO simulation results, and the dashed lines indicate the values assigned by AMBER03. Simulated results, represented by the solid line, were employed for the molecular force field.

obtain the saturated liquid density of the bulk, based on these results, equilibration and sampling times were considered sufficient.

Fig. 5(a) and Fig. 5(c) compare the saturation pressure and vapor–liquid coexistence curve, respectively, of the measurement data and MD simulation for R1132(E). Fig. 5(b) and Fig. 5(d) show the deviation based on the proposed equations with respect to the saturation pressure and vapor–liquid coexistence curves, respectively. Perera et al. [14] provided measurement data for the saturation pressure at temperatures from 240 K to the critical point and proposed a Wagner-type correlation based on their measurement data. The simulated saturation pressure (~50 kPa) agreed well with the experimental data. The perturbed chain statistical associating fluid theory (PC-SAFT) equation of state [54]

Table 4
Bonded interaction parameters adopted in MD simulation for R1132(E) and R1132a.

	Bond	r_0 [nm]	k_r [kJ mol^{-1} nm^{-2}]	Angle	θ_0 [°]	k_θ [kJ mol^{-1} rad^{-2}]
R1132(E)	C=C	0.132821	303324	H–C=C	125.721	218.52
	C–F	0.135402	193283	F–C=C	119.725	332.09
	C–H	0.108078	181460	H–C–F	114.554	291.50
R1132a	C=C	0.132268	307586	H–C=C	119.66	199.07
	C–F	0.132957	206755	F–C=C	125.19	388.14
	C–H	0.107932	182281	H–C–H	120.68	195.07
				F–C–F	109.63	555.13

*dihedral angle parameters assigned by AMBER03 [22]: $k_\phi = 27.82360$ kJ mol^{-1} and $\phi_0 = 180°$.

Table 5
Non-bonded interaction parameters adopted in MD simulation for R1132(E) and R1132a.

	Atom #*	Atom	Partial charge	LJ parameters	
			q [C]	σ [nm]	ε [kJ/mol]
R1132(E)	1	C	−0.029726e	0.3400	0.410000
	2	H	0.218171e	0.2500	0.085000
	3	C	−0.029726e	0.3400	0.410000
	4	H	0.218171e	0.2500	0.085000
	5	F	−0.188444e	0.2900	0.255224
	6	F	−0.188444e	0.2900	0.255224
R1132a	1	C	−0.819413e	0.3620	0.410000
	2	H	0.297352e	0.2450	0.064500
	3	C	0.652199e	0.3520	0.380000
	4	F	−0.213745e	0.2900	0.223000
	5	F	−0.213745e	0.2900	0.223000
	6	H	0.297352e	0.2450	0.064500

*Atom # corresponds to the number designated in Fig. 1(a).

enables the saturation pressure calculation for R1132(E) and R1132a, with parameters correlated by Anoune et al. [55]. The parameters used in this study, calculated using their correlation, are listed in Table 6. The critical parameters and acentric factors used, in addition to those in Table 6, are presented in Table 1. The saturation pressure of R1132(E) given by the PC-SAFT equation of state was in excellent agreement with the measured results and correlation of Perera et al. In contrast, Sakoda et al. measured the saturated vapor and liquid densities from 317 K to the critical point [8]. Since the only previously reported measurements were their 19 data, additional density data were obtained using an apparatus identical to that used by Sakoda et al. Details of these data are provided in Appendix E. Although these two density data series were measured for samples obtained at different times, they were highly reproducible. The Lennard–Jones parameters, ε and σ, of the force field used in the MD simulation were adjusted to match the measurement data, resulting in the saturated liquid density agreeing within approximately 2 % at temperatures above 300 K. Using the molecular force field, the simulation range was lowered to 200 K (plotted with red symbols in Fig. 5). Sakoda et al. proposed optimized coefficients for the Penterman–Wagnar equation [56], indicated by a solid blue line in Fig. 5 (c) and 5(d). However, this equation indicates that the saturated liquid density is significantly lower than the liquid density given by the Peng–Robinson equation of state [57] at temperatures below 300 K, for which no experimental data are available. If the additional liquid density at 307.23 K measured here had been determined, their Penterman–Wagnar type equation would have predicted values much closer to the MD simulation and Peng-Robinson equation of state. The saturated vapor density predicted by the PC-SAFT equation of state agrees well with the other data up to the critical point temperature; however, the saturated liquid density has been significantly underpredicted. Anoune et al. [55] explained this by stating that they opted to prioritize the accuracy of saturation pressure over the precision of liquid density prediction when proposing parameter correlations. A comparison with the volume-translated Peng–Robinson equation of state [58], which improves the calculation accuracy on the saturated liquid side, showed good agreement with the measurements of Higashi and Sakoda et al. and the MD simulations down to 200 K. The volume-translated Peng–Robinson equation of state (VT-PR), shown by a green line in Fig. 5(c) and 5(d), agrees with the measured and simulated liquid densities from the critical point to 200 K without any adjustment. However, VT-PR was approximately 2 % higher than the other data in Fig. 5(d). The solid purple lines in Fig. 5 (c) and Fig. 5(d) show the following Hankinson–-Thomson correlation [59].

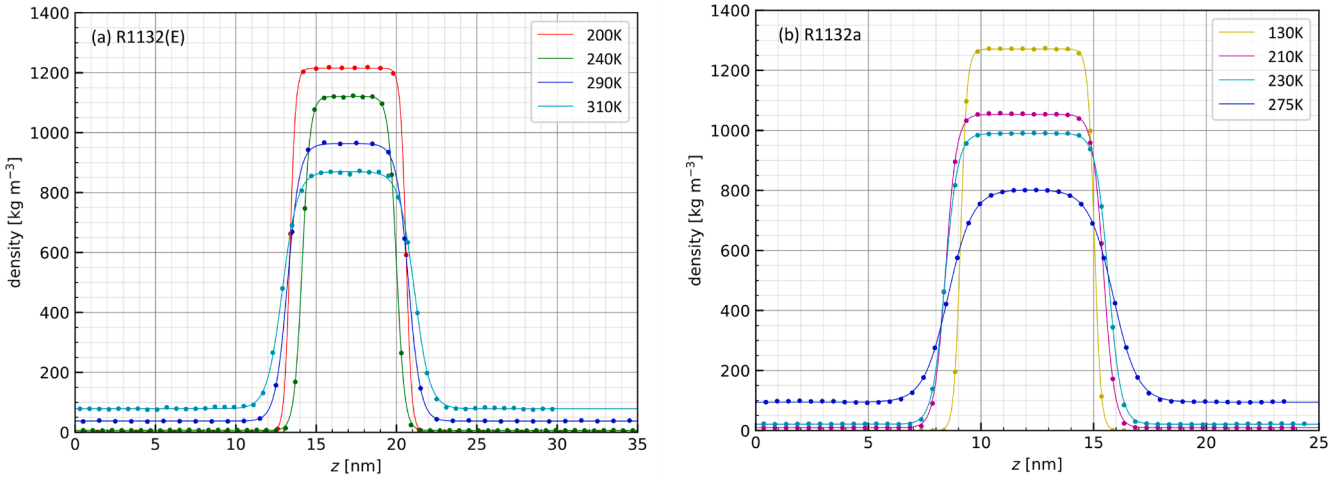

Fig. 4. Density distribution in the z-direction obtained by MD simulation (symbols) and the profile represented by Eq. (3) (lines) at various saturation temperatures for (a) R1132(E) and (b) R1132a.

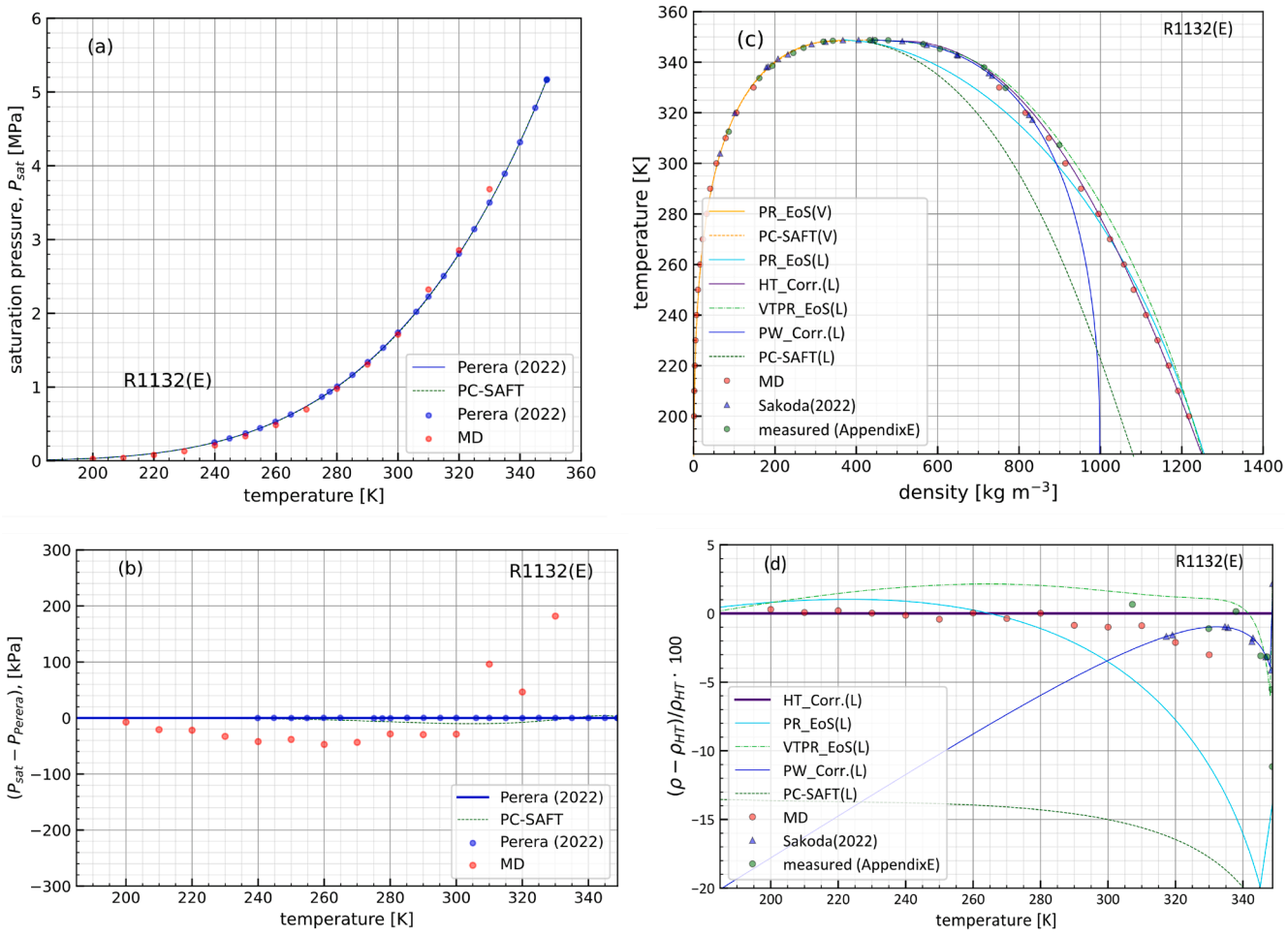

Fig. 5. Comparison of the R1132(E) saturation properties obtained by measurement and simulation. (a) Saturation pressure, (b) deviation in the saturation pressure based on the correlation, (c) vapor–liquid coexistence curve, and (d) deviation in the saturated liquid density based on the Hankinson–Thomson correlation [59]. In (a) and (b), lines denote the Wagner-type correlation optimized by Perera et al. [14] and PC-SAFT equation of state [54] with parameters correlated by Anoune et al. [55]. Symbols represent the measurement data obtained by Perera et al. [20] and molecular simulation results. In (c) and (d), lines denote the Peng–Robinson equation of state for vapor and liquid phases (PR_EoS(V) and PR_EoS(L)) [57], PC-SAFT equation of state (PC-SAFT(V) and PC-SAFT(L)), VT-RP equation of state (VT-PR-EoS) [58], slightly adjusted Hankinson–Thomson correlation Eq. (10) (HT_Corr.(L)) [59], and Pentermann–Wagnar correlation (PW_Corr.(L)) [56] optimized by Sakoda et al. [8]. Symbols represent the MD simulation results, data measured by Sakoda et al. [8], and additional data measured in this study using the same apparatus as Sakoda et al. (the data measured in this study is listed in Appendix E).

$$
\begin{aligned}
&\rho^{'} = (1000MM)/[v_{\mathrm{crit}} v_{\mathrm{R0}} (1 - \omega v_{\mathrm{R}\delta})],\\
&v_{\mathrm{R0}} = 1 - 1.52816\tau^{1/3} + 1.43907\tau^{2/3} - 0.81446\tau + 0.190454\tau^{4/3},\\
&v_{\mathrm{R}\delta} = \left(-0.296123 + 0.386914T_{\mathrm{R}} - 0.0427258T_{\mathrm{R}}^{2} - 0.0480645T_{\mathrm{R}}^{3} \right)/(T_{\mathrm{R}} - 1.00001),\\
&\tau = 1 - T_{\mathrm{R}}, v_{\mathrm{crit}} = 1000 \cdot MM/\rho_{\mathrm{crit}}
\end{aligned}
\tag{9}
$$

Tanaka et al. [60] successfully calculated the saturation density of another HFO R1336mzz(E), with high accuracy using this method. To accurately represent the measured and simulated liquid densities from the critical point to 200 K, the coefficient of v_{R0} needs to be slightly adjusted as follows:

$$v_{\mathrm{R0}} = 1 - 1.524\tau^{1/3} + 1.43907\tau^{2/3} - 0.81446\tau + 0.190454\tau^{4/3} \tag{10}$$

This adjusted Hankinson–Thomson correlation was used to obtain the surface tension using Eq. (8) and the differential capillary rise method.

Similar to R1132(E), the saturation pressure and vapor–liquid coexistence curve are plotted for R1132a in Fig. 6. As shown in Fig. 6(a) and 6(b), the saturation pressure data were provided by Kayukawa et al. [61] down to approximately 175 K. All the measurement data from near the critical point to 175 K were consistent and well represented by the Wagner correlation (with coefficients proposed by Thu et al. [62]) and PC-SAFT equation of state [54] (with parameters correlated by Anoune et al. [55]). The pressure simulated by MD was 100 kPa higher than the correlation above 250 K. Nevertheless, the other data below 250 K agreed with the correlation within 50 kPa. The measured saturation densities were provided from the critical point to approximately 180 K for R1132a, and all data were consistent. The saturated liquid densities obtained by the MD simulation also agree with the measurements within 1 %. The saturated vapor density calculated by the PC-SAFT equation of state, which is significantly smaller, agrees well with the measured

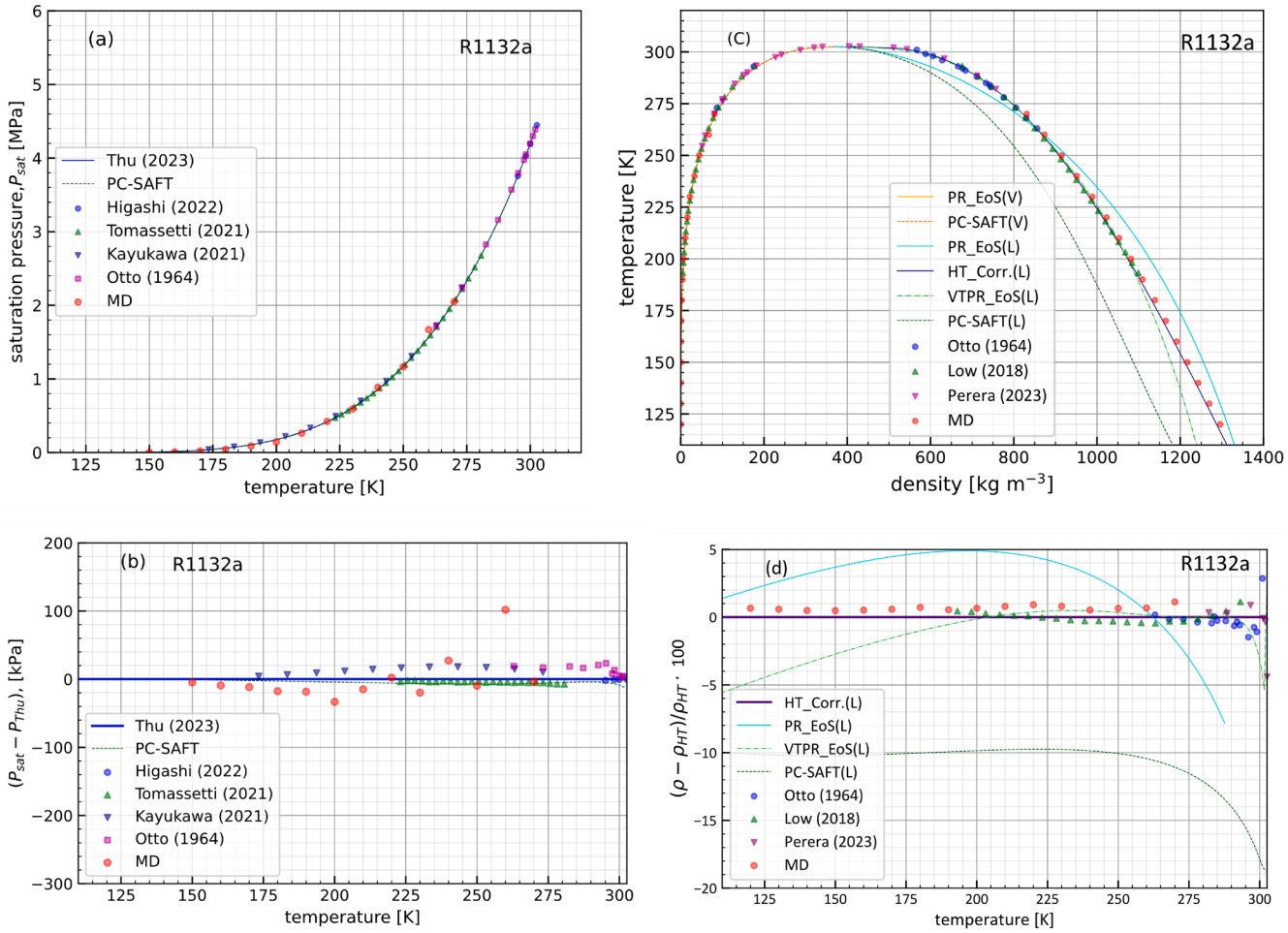

Fig. 6. Comparison of the saturation properties of R1132a obtained by measurement and simulation. (a) Saturation pressure, (b) deviation in the saturation pressure based on Thu's correlation, (c) vapor–liquid coexistence curve, and (d) deviation in the saturated liquid density based on the Hankinson–Thomson correlation [59]. In (a) and (b), lines denote the Wagner-type correlation with the optimized coefficient by Thu et al. [49] and PC-SAFT equation of state [54] with parameters correlated by Anoune et al. [55]. Symbols represent the data measured by Higashi [63], Tomasetti and Di Nicola [64], Kayukawa et al. [61], and Otto and Thomas [65]. In (c) and (d), lines denote the Peng–Robinson equation of state for vapor and liquid phases (PR_EoS(V) and PR_EoS(L)) [57], PC-SAFT equation of state for vapor and liquid phases (PC-SAFT(V) and PC-SAFT(L)), VT-PR-EoS [58], and slightly adjusted Hankinson–Thomson correlation Eq. (11) (HT_Corr.(L)) [59]. Symbols represent measured by density data obtained by Otto and Thomas [52], Low [53], Perera et al. [16], and the MD simulation results.

Table 6
Parameters used in the PC-SAFT equation of state for R1132(E) and R1132a, correlated by Anoune et al. [55].

	Segment number	Segment diameter nm	Potential depth kJ/mol
R1132(E)	2.8628	0.30005	1.361
R1132a	2.3223	0.32415	1.299

value. The VT-PR-EoS agrees well with the measured saturation density from the critical point to 200 K. However, below 200 K, the VT-PR-EoS indicates a lower saturated liquid density than the MD simulation. Although the Hankinson–Thomson correlation well represented the variation in liquid density down to 120 K, a slight adjustment of the v_{R0} coefficient was required to match the MD values below 200 K by 1 %, as given in the following formula:

$$v_{R0} = 1 - 1.52816\tau^{1/3} + 1.43907\tau^{2/3} - 0.81446\tau + 0.18\tau^{4/3} \quad (11)$$

The adjusted Hankinson–Thomson correlation is substituted as the ρ' value in Eq. (8) to measure the surface tension using the differential capillary rise method.

4.4. Surface tension and parachor

Fig. 7 plots the surface tension measured by the differential capillary rise method and parachor determined for R1132(E). The measurements were repeated five times on different dates with recharged samples. As shown in Fig. 7(b), the five series of measured data agree within the uncertainty range indicated by the vertical bars. The following van der Waals-type empirical equation, indicated by a solid blue line and judged to be sufficiently reproducible, was obtained for R1132 (E) from the measurement data.

$$\gamma = 66.65(1 - T/T_{crit})^{1.22} \ [\mathrm{mNm^{-1}}] \quad (12)$$

Here, T_{crit} denotes the critical temperature (348.82 K) [8]. The coefficient and exponent were determined by least-squares method to be representative of the measured surface tension within 0.25 mNm^{-1}, which is slightly larger than the evaluated uncertainty. The surface tension simulated by MD, shown with the red circle, is approximately 0.5 mNm^{-1} lower than that given by the empirical correlation. Although the MD simulation results are generally lower than the measured surface tension, they vary widely by approximately 0.5 mNm^{-1}. Di Nicola et al. [66–68]and Miqueu et al. [69], derived by regression analysis and other methods from experimental values, predict a somewhat lower surface

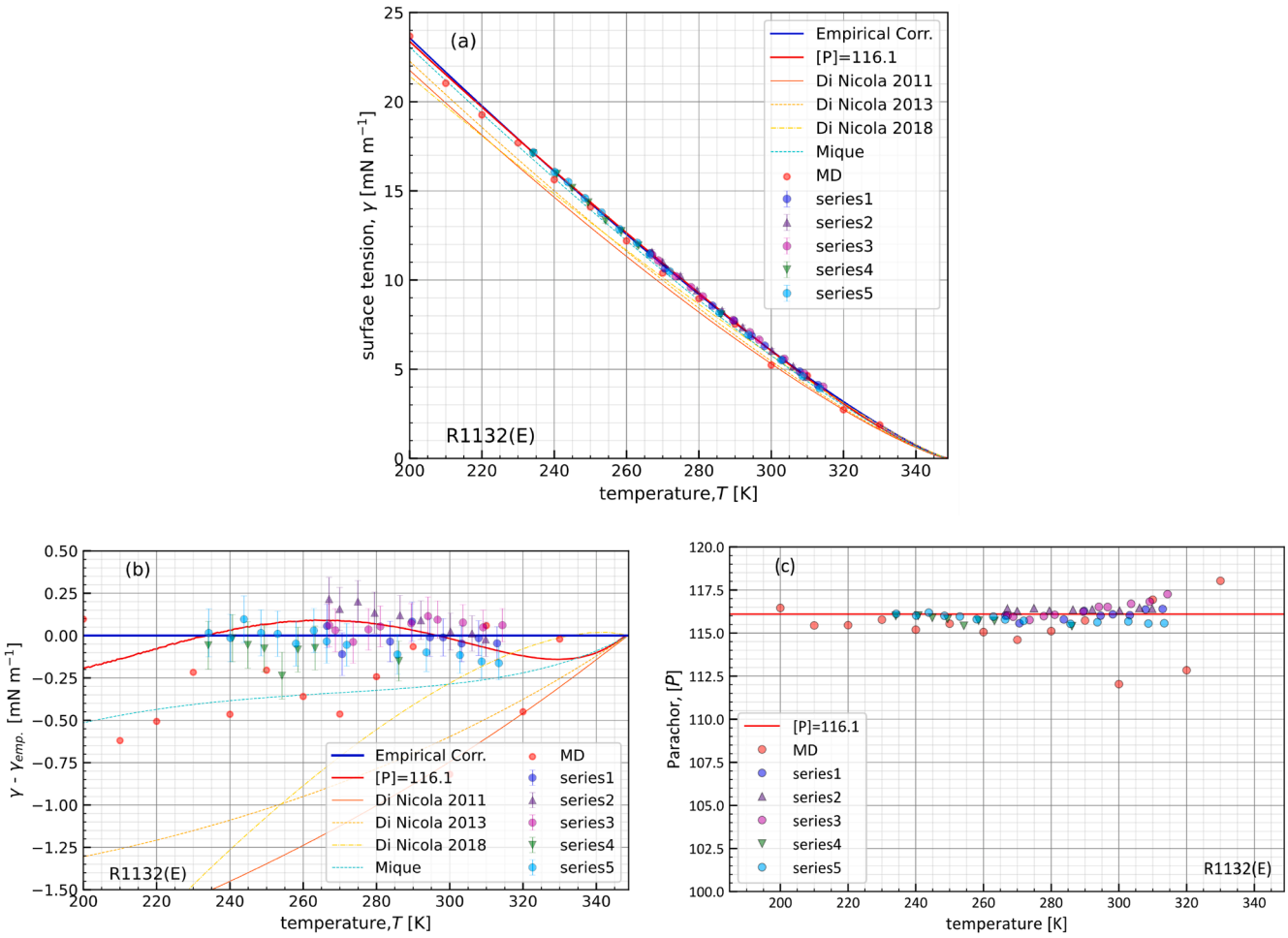

Fig. 7. Measured and simulated surface tension and parachor for R1132(E). (a) Temperature dependence of surface tension, (b) deviation in surface tension based on the van der Waals-type empirical correlation (Eq. (12)), and (c) parachors obtained using the measured or simulated surface tension, calculated density by Peng–Robinson equation of state for saturated vapor [57], and adjusted Hankinson–Thomson correlation [59] for saturated liquid. Red circles indicate MD simulation. Circle symbols with vertical bars indicate the five series of measurement data and their measurement uncertainties. Solid blue lines show the empirical correlation obtained based on the measurements. Solid red lines show the calculation results, obtained using the parachor method with an averaged parachor [P] of 116.1. The dashed lines show the predicted surface tensions of Di Nicola et al. [66–68] and Miqueu et al. [69]. (For interpretation of the references to colour in this figure legend, the reader is referred to the web version of this article.)

tension (plotted with dashed lines) than the measured value. Among the selected predictions, the predictions of Miqueu et al. were the closest value to the measurement, agreeing with the 0 ∼ −0.5 mNm^{-1} range.

The parachor was determined from the measured surface tension and calculated density, as shown in Fig. 7(c), using the following correlation. The parachor method was developed empirically by Macleod [70], who established a remarkably simple relation between the saturated densities of liquids and vapors and their surface tension. This was written by Sugden [71] in terms of molar densities ($\tilde{\rho}'$ and $\tilde{\rho}''$ (mol cm^{-3})) as

$$\gamma = \{[P](\tilde{\rho}' - \tilde{\rho}'')\}^{\pi} \tag{13}$$

where [P] denotes a substance-specific value parameter. Later, Fowler [72] and Boudh-Hir and Mansoori [73] attempted to rationalize this simple correlation using statistical mechanics. In these studies, a scaling exponent (π) of 4 was determined. However, Garrabos's theoretical analysis [74] recommends 3.87. However, Zhelezny et al. [75] noticed that an exponent of 3.88 shows a more obvious temperature dependence in the parachor near the critical point than that of 4.00. Although the exponent remains controversial, a conventional scaling exponent of four was selected for this study. The parachor of R1132(E) is determined by averaging the five data series shown in Fig. 7(c). However, because the surface tension measurement uncertainty was significant above 300 K, and the parachor data were scattered, the data below 300 K were weighted, and the averaged parachor was determined as 116.1 for R1132(E). The surface tension of R1132 (E) calculated using the parachor method is indicated by the solid red line in Fig. 7(a). As shown in Fig. 7(b), the measured values and empirical equations agree within 0.25 mNm^{-1} from 200 K to the critical temperature. The parachors, calculated from the surface tension of the MD simulation and densities of the Hankinson–Thomson correlation, indicated by the red circles, were generally 116 K – 200 K. The calculated saturated density, measured surface tension, uncertainties, and parachor data are summarized in Table 7. The capillary constants, defined in Eq. (7) is added so that the surface tension can be recalculated from the saturation density with greater accuracy when an advanced equation of state based on a wide range of measured properties is provided.

Fig. 8(a) shows the temperature dependence of the surface tension of R1132a. The measurement results of series 1 and 2 agree within the measurement uncertainty. The data in series 3 showed more variability than those in series 1 and 2 because of the lower precision of temperature control using liquid nitrogen. Nevertheless, data at low temperatures, down to approximately 220 K, are essential references for proposing empirical formulas and determining the parachor- and van der Waals-type empirical equations for these three series.

Table 7
Saturated vapor and liquid densities calculated using Peng-Robinson equation of state and Hankinson-Thomson correlation with Eq. (10), measured capillary constant, surface tension, and parachor for R1132(E).

Date	Temperature (ITS-90) T [K]	Vapor density ρ" [kg/m^3]	Liquid density ρ' [kg/m^3]	Capillary constant a^2 [mm^2]	Surface tension γ [mN/m]	Measurement uncertainty U_γ [mN/m]	Obtained parachor [P]
Series 1 (sample purity > 99.6 %)							
20190115	289.71	43.73	961.78	1.72	7.73	0.12	116.29
20190116	294.59	50.31	943.92	1.57	6.87	0.11	116.01
20190116	298.19	55.73	930.21	1.47	6.32	0.11	116.09
20190116	303.22	64.25	910.18	1.33	5.52	0.11	116.04
20190116	307.89	73.27	890.54	1.22	4.87	0.10	116.37
20190116	312.92	84.47	867.95	1.07	4.11	0.10	116.40
20190117	270.62	24.63	1025.45	2.17	10.64	0.13	115.57
20190117	283.73	36.71	982.69	1.85	8.56	0.12	115.79
20190118	266.51	21.61	1038.12	2.31	11.50	0.13	116.02
Series 2 (sample purity > 99.6 %)							
20190204	292.13	46.88	953.04	1.66	7.35	0.11	116.37
20190205	300.20	59.00	922.34	1.43	6.05	0.11	116.31
20190205	309.81	77.36	882.09	1.16	4.58	0.10	116.42
20190205	306.07	69.62	898.30	1.27	5.16	0.10	116.46
20190205	286.43	39.74	973.39	1.81	8.28	0.12	116.36
20190206	267.05	21.99	1036.47	2.33	11.57	0.13	116.42
20190206	269.96	24.13	1027.47	2.24	11.02	0.13	116.28
20190206	274.91	28.15	1011.86	2.13	10.24	0.12	116.44
20190207	279.49	32.35	996.94	1.99	9.42	0.12	116.30
Series 3 (sample purity > 99.6 %)							
20190313	289.48	43.43	962.62	1.72	7.75	0.12	116.25
20190313	294.08	49.58	945.83	1.61	7.07	0.11	116.52
20190313	303.61	64.96	908.56	1.35	5.59	0.11	116.70
20190314	314.37	88.02	861.14	1.06	4.02	0.10	117.26
20190314	309.11	75.84	885.18	1.20	4.75	0.10	116.82
20190314	296.68	53.39	936.04	1.54	6.65	0.11	116.51
20190314	281.04	33.89	991.79	1.94	9.09	0.12	116.06
20190315	267.12	22.04	1036.24	2.30	11.40	0.13	116.03
20190315	268.77	23.23	1031.17	2.25	11.10	0.13	115.95
20190315	273.61	27.04	1016.01	2.11	10.22	0.12	115.76
20190315	277.81	30.75	1002.46	2.02	9.60	0.12	115.99
Series 4 (sample purity > 99.9 %)							
20200106	286.12	39.38	974.47	1.76	8.06	0.12	115.40
20200108	263.24	19.43	1047.97	2.37	11.93	0.13	115.71
20200108	258.55	16.62	1061.84	2.49	12.73	0.13	115.72
20200108	254.21	14.31	1074.39	2.57	13.33	0.14	115.42
20200109	249.38	12.06	1088.02	2.72	14.34	0.14	115.81
20200109	244.89	10.22	1100.44	2.84	15.16	0.14	115.90
20200109	240.71	8.72	1111.81	2.95	15.95	0.14	116.01
20200110	234.11	6.70	1129.36	3.11	17.10	0.14	116.00
Series 5 (sample purity > 99.9 %)							
20200114	285.72	38.93	975.84	1.78	8.17	0.12	115.54
20200114	271.89	25.63	1021.46	2.15	10.49	0.13	115.71
20200115	266.41	21.54	1038.43	2.29	11.43	0.13	115.79
20200115	262.92	19.23	1048.94	2.40	12.09	0.13	115.96
20200115	258.02	16.32	1063.37	2.51	12.85	0.13	115.80
20200116	253.02	13.73	1077.75	2.65	13.78	0.13	115.96
20200116	248.49	11.67	1090.51	2.76	14.59	0.14	116.01
20200116	243.84	9.83	1103.31	2.89	15.50	0.14	116.19
20200117	240.12	8.52	1113.39	2.97	16.06	0.14	116.02
20200117	234.22	6.73	1129.05	3.12	17.16	0.14	116.12
20200120	293.64	48.95	947.48	1.57	6.93	0.11	115.63
20200120	302.78	63.45	911.98	1.33	5.52	0.11	115.67
20200120	308.70	74.98	886.97	1.16	4.61	0.10	115.56
20200120	313.40	85.62	865.72	1.03	3.93	0.10	115.57

$$\gamma = 56.37(1 - T/T_{crit})^{1.26}\ [\mathrm{mNm^{-1}}] \quad (14)$$

Here, the critical temperature T_{crit} was 302.62 K [7]. As plotted in Fig. 8 (b), this correlation represents the measurement data within ± 0.5 mNm^{-1} and agrees well with the MD simulation at temperatures down to the triple point. The literature data reported for DIPPR [76] and DETHERM [77] are considerably higher than the present data at low temperatures, probably because they are estimated based on other measured properties or numerical analyses such as MD. This anomaly in the literature values of R1132a was also found in a study by Di Nicola et al. [54], where HFO refrigerant surface tensions were compared comprehensively. The dashed lines in Fig. 8(a) and 8(b) represent the predicted correlation, which yields a lower surface tension than the measured value. Di Nicola et al. [68] reported slightly higher values from 180 K to the critical point, which were in good overall agreement. Because the measurements were performed at reduced temperatures above 0.76 for R1132a, the calculated parachor, shown in Fig. 8(c), was highly scattered. Therefore, the parachor was determined as 116.7 by weighting the data at lower temperatures and referring to the MD value. The obtained parachor was close to that of the isomer R1132(E) (116.1), indicating that parachor is predominantly dependent on the constituent atoms. As compared in Fig. 8(b), the surface tension calculated by the parachor method with [P] = 116.7 represents the measured surface tension within 0.5 mNm^{-1}, which is comparable to the variation range of the measurement data. Although less accurate than those in the R1132(E) case, the saturated density and surface tension measurements

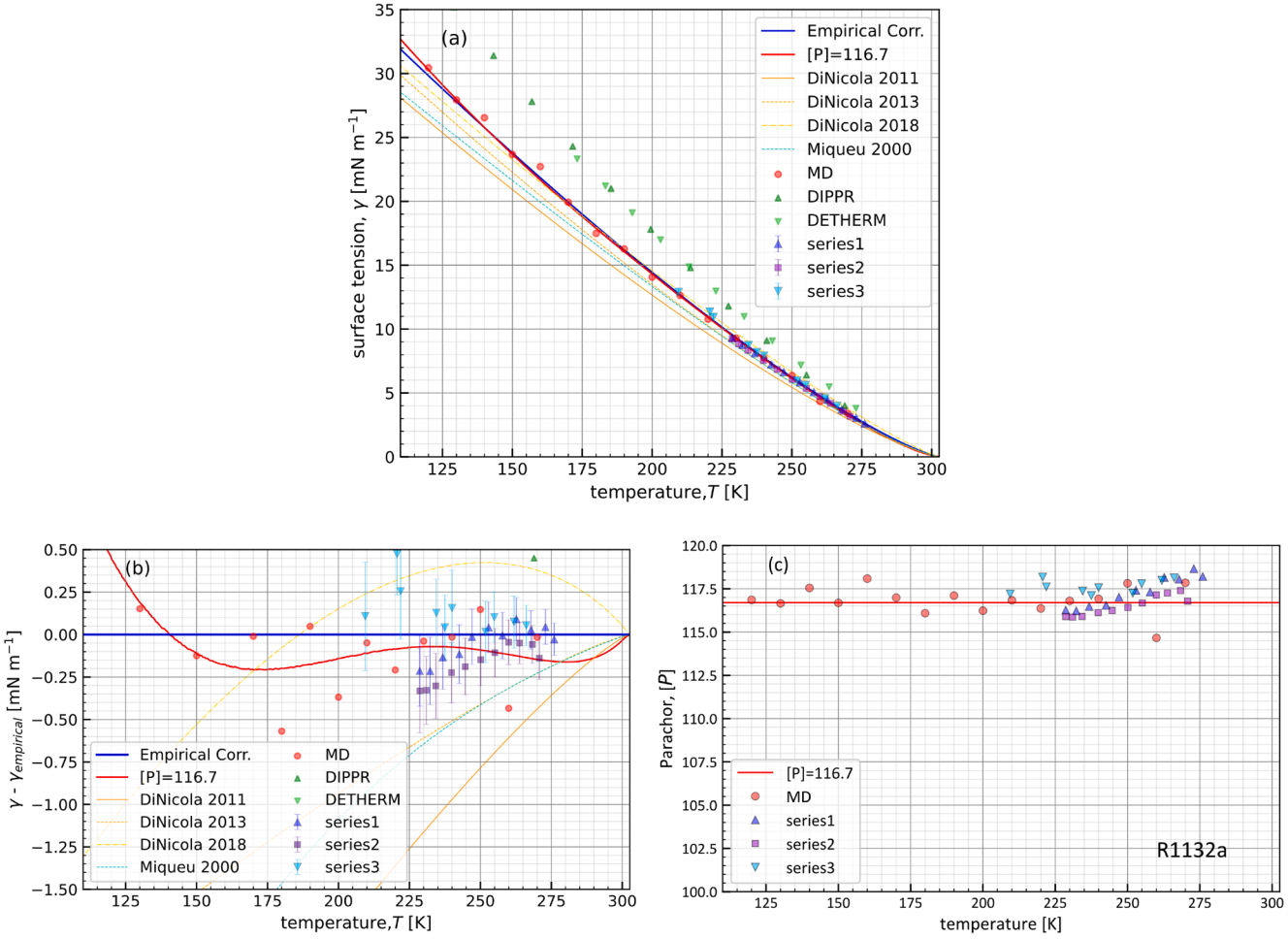

Fig. 8. Surface tension and parachor measured and simulated for R1132a. (a) Temperature dependence of surface tension, (b) deviation in surface tension based on the van der Waals-type empirical correlation (Eq.(14)), and (c) parachor obtained using the measured or simulated surface tension, calculated density by Peng-Robinson equation of state for saturated vapor [43], and adjusted Hankinson-Thomson correlation [45] for saturated liquid. Red circles represent the MD simulation results. Green triangles and inverted triangles represent data reported in DIPPR [76] and DETHERM [77]. Symbols with vertical bars represent three series of present measurement data. The thick solid blue and red lines indicate the empirical correlation and parachor method with [P] = 116.7, respectively. The thin lines show the surface tensions predicted by Di Nicola et al. [53–55] and Miqueu et al. [56]. (For interpretation of the references to colour in this figure legend, the reader is referred to the web version of this article.)

supplemented by MD in the low-temperature range are in accordance with empirical laws and show no noticeable discrepancies. The aforementioned surface tension measurements, their uncertainties, and the obtained parachor data are detailed in Table 8.

5. Conclusions

The surface tensions of R1132(E) and its isomer R1132a were measured using the differential capillary rise method assisted by molecular simulation. Molecular orbital simulations were performed to calculate the equilibrium bond lengths and bond angles, and atomic charges were assigned to establish the force field. The simulated equilibrium bond lengths agreed with those obtained by the general force field AMBER03. However, the simulated bond angles deviated somewhat from those of AMBER03, probably due to the steric hindrance of the π-bonds. The Lennard–Jones parameters were adjusted using highly accurate saturation density measurement data near the critical point. Molecular dynamics simulations were performed using the force fields established for R1132(E) and R1132a to represent a vapor–liquid equilibrium system close to the triple point. The saturated liquid density was correlated using the Hankinson–Thomson correlation, which was slightly adjusted to fit the measured and simulated data seamlessly from the critical point to the triple point.

The surface tension and parachor were obtained from the measured difference in the capillary rise height, with the saturation densities correlated to the temperatures from 225 K to that near the critical point. However, for the measurements of R1132a at temperatures as low as ~ 209 K, measurement data with temperature control using liquid nitrogen were also provided. Although the measurement uncertainty was significant owing to the difficulty of temperature control, these data were referenced to propose highly reliable empirical correlations and parachors. The proposed van der Waals-type empirical correlations are as follows:

$$\gamma = 66.65(1 - T/348.82)^{1.22}[\mathrm{mNm^{-1}}] \text{ for } R1132(\mathrm{E})$$

$$\gamma = 56.37(1 - T/302.62)^{1.26}[\mathrm{mNm^{-1}}] \text{ for } R1132a.$$

The proposed parachors are $[P] = 116.1$ for R1132(E) and $[P] = 116.7$ for R1132a. These values are similar, implying that the value of the parachor is predominantly dependent on the constituent atoms. The proposed empirical equation is representative of the R1132(E) and R1132a measurements within 0.25 and 0.5 $\mathrm{mNm^{-1}}$, respectively. The surface tension calculated from the proposed parachors and saturated liquid density of adjusted Hankinson–Thomson correlation agreed with

Table 8
Saturated vapor and liquid densities calculated using the Peng-Robinson equation of state and Hankinson-Thomson correlation with Eq. (11), measured capillary constant, surface tension, and parachor for R1132a.

Date	Temperature (ITS-90) T [K]	Vapor density ρ'' [kg/m^3]	Liquid density ρ' [kg/m^3]	Capillary constant a^2 [mm^2]	Surface tension γ [mN/m]	Measurement uncertainty U_γ [mN/m]	Obtained parachor [P]
Series 1							
20221129	252.89	49.62	897.26	1.41	5.83	0.15	117.41
20221129	242.58	35.74	936.70	1.64	7.23	0.17	116.54
20221129	232.28	25.39	973.01	1.89	8.75	0.20	116.23
20221130	228.63	22.39	985.33	1.98	9.34	0.21	116.26
20221130	236.75	29.52	957.56	1.79	8.12	0.19	116.48
20221130	247.06	41.27	920.00	1.54	6.65	0.16	117.01
20221130	257.82	57.85	877.03	1.26	5.07	0.14	117.31
20221130	262.68	67.23	855.95	1.16	4.49	0.13	118.16
20221130	267.81	78.77	832.24	1.01	3.72	0.11	118.06
20221130	272.93	92.39	806.68	0.88	3.07	0.10	118.66
20221130	276.02	101.85	790.11	0.77	2.61	0.09	118.21
Series 2							
20230529	259.93	61.76	868.01	1.20	4.73	0.13	117.15
20230529	255.11	53.17	888.29	1.31	5.36	0.14	116.68
20230530	228.67	22.42	985.20	1.96	9.22	0.25	115.90
20230530	230.98	24.29	977.42	1.89	8.85	0.20	115.86
20230530	234.29	27.19	966.11	1.81	8.34	0.19	115.90
20230530	239.83	32.68	946.64	1.69	7.55	0.18	116.12
20230530	244.66	38.23	928.99	1.57	6.84	0.17	116.24
20230530	250.13	45.49	908.19	1.43	6.05	0.15	116.43
20230530	263.79	69.58	850.93	1.10	4.19	0.12	117.26
20230531	268.33	80.05	829.75	0.97	3.57	0.11	117.40
20230531	270.78	86.40	817.64	0.88	3.16	0.12	116.78
Series 3 (temperature controlled by liquid nitrogen)							
20240109	251.8	48.00	901.47	1.42	5.96	0.18	117.24
20240109	266.2	74.83	840.09	1.05	3.97	0.12	118.14
20240111	254.9	52.83	889.14	1.36	5.60	0.15	117.79
20240111	237.5	30.25	954.97	1.80	8.18	0.19	117.11
20240111	240.0	32.86	946.03	1.76	7.90	0.22	117.56
20240116	261.9	65.55	859.58	1.17	4.58	0.15	117.99
20240116	234.5	27.36	965.44	1.90	8.74	0.20	117.37
20240116	209.4	11.02	1046.25	2.54	12.89	0.32	117.20
20240116	220.6	16.85	1011.38	2.33	11.35	0.24	118.18
20240116	221.9	17.64	1007.34	2.25	10.92	0.28	117.62

the R1132(E) and R1132a measurement data within 0.25 and 0.5 mNm^{-1}, respectively.

CRediT authorship contribution statement

Tomoaki Imai: Software, Methodology, Investigation. **Takemasa Kawahara:** Validation, Methodology, Investigation. **Ryutaro Nonaka:** Data curation. **Sebastiano Tomassetti:** Methodology, Formal analysis. **Tetsuya Okumura:** Supervision, Methodology. **Yukihiro Higashi:** Validation, Investigation. **Giovanni DI Nicola:** Supervision. **Chieko Kondou:** Writing – original draft, Supervision, Funding acquisition.

Declaration of competing interest

The authors declare the following financial interests/personal relationships which may be considered as potential competing interests: Chieko Kondou reports financial support was provided by Japan Science and Technology Agency.

Data availability

Data will be made available on request.

Acknowledgments

Daikin Industries Ltd. provided high-purity samples of R1132(E) and R1132a free of charge. The Japan Science and Technology Agency funded the molecular simulation study through the “Fusion Oriented Research for Disruptive Science and Technology (FOREST)” fund (No. JPMJFR2172). The authors are grateful for this support.

Appendix

The mol2 file, which describes the molecular structure and atomic charges obtained from the structural optimization calculations, and topology file used in the molecular simulations with Gromacs are shown in Appendices A–D. Appendix E lists the measured saturation density for R1132(E), as obtained in this study.

Appendix A. R1132(E) mol2 file

@<TRIPOS > MOLECULE				
MOL				
6	5	1	0	0
SMALL				
USER_CHARGES				

@<TRIPOS > ATOM					
1 C1	−0.337000000	0.572000000	0.000000000C.2	1 MOL	−0.029726000
2 H1	−1.413000000	0.672000000	0.000000000H	1 MOL	0.218171000
3 C2	0.337000000	−0.572000000	0.000000000C.2	1 MOL	−0.029726000
4 H2	1.413000000	−0.672000000	0.000000000H	1 MOL	0.218171000
5 F1	−0.337000000	−1.747000000	0.000000000F	1 MOL	−0.188444000
6 F2	0.337000000	1.747000000	0.000000000F	1 MOL	−0.188444000

@<TRIPOS > BOND		
1	1	2 1
2	1	3 2
3	1	6 1
4	3	4 1
5	3	5 1

@<TRIPOS > SUBSTRUCTURE		
1	MOL	1
@<TRIPOS > COMMENT		

Appendix B. R1132(E) Gromacs topology file

```
; Topology files based on OPLS/AA-L and AMBER03 customized for R1132(E) available on Gromacs
; Details are given in the paper:
; T. Imai, T. Kawahara, R. Nonaka, S. Tomassetti, T. Okumura, Y. Higashi, G. Di Nicola, C. Kondou
; “Surface Tension Measurement and Molecular Simulation for New Low Global Warming Potential
; Refrigerants R1132(E) and R1132a”
;Journal of Molecular Liquids
```

[defaults].

; nbfunc	comb-rule	gen-pairs	fudgeLJ	fudgeQQ
1	2	yes	0.5	0.5

[atomtypes].

;name	at.num	mass	charge	ptype	sigma	epsilon	Amb
C_01	6	0.0	0.0	A	0.3400	0.410000	
H_01	1	0.0	0.0	A	0.2500	0.085000	
C_01	6	0.0	0.0	A	0.3400	0.410000	
H_01	1	0.0	0.0	A	0.2500	0.085000	
F_01	9	0.0	0.0	A	0.2900	0.255224	
F_01	9	0.0	0.0	A	0.2900	0.255224	

[moleculetype].

;name	nrexcl
MOL01 3	

[atoms].

;nr	type	resi	res	atom	cgnr	charge	mass
1	C_01	1	MOL01	C1	1	−0.029726	12.01100
2	H_01	1	MOL01	H2	2	0.218171	1.00800
3	C_01	1	MOL01	C3	3	−0.029726	12.01100
4	H_01	1	MOL01	H4	4	0.218171	1.00800
5	F_01	1	MOL01	F5	5	−0.188444	18.99840
6	F_01	1	MOL01	F6	6	−0.188444	18.99840

[bonds].

;ai	aj	funct	r	k
1	2	1	1.08078e-01	1.81460e+05
1	3	1	1.32821e-01	3.03324e+05
1	6	1	1.35402e-01	1.93283e+05
3	4	1	1.08078e-01	1.81460e+05
3	5	1	1.35402e-01	1.93283e+05

[pairs].

2	4	1
2	5	1
6	4	1
6	5	1

[angles].

;ai	aj	ak	funct	theta	cth
1	3	4	1	1.25721e+02	2.1852e+02
1	3	5	1	1.19725e+02	3.3209e+02
2	1	3	1	1.25721e+02	2.1852e+02
2	1	6	1	1.14554e+02	2.9150e+02
3	1	6	1	1.19725e+02	3.3209e+02
4	3	5	1	1.14554e+02	2.9150e+02

[dihedrals].

2	1	3	4	9	180.00	27.82360	2
2	1	3	5	9	180.00	27.82360	2
6	1	3	4	9	180.00	27.82360	2
6	1	3	5	9	180.00	27.82360	2
1	5	3	4	4	180.00	4.60240	2
2	1	6	3	4	180.00	4.60240	2

[system].
R1132E_CCSD/DGTZVP_RESP calculated on 2023 Oct. 14 by C. Kondou.
Intra-molecular FF optimized by T. Imai on 2023 Oct. 23.
[molecules].
MOL01 3000

Appendix C. R1132a mol2 file

@<TRIPOS > MOLECULE				
MOL				
6	5	1	0	0
SMALL				
USER_CHAGES				

@<TRIPOS > ATOM					
1 C1	0.000000000	0.000000000	1.390000000C.2	1 MOL	−0.819413000
2 H1	0.000000000	0.938000000	1.924000000H	1 MOL	0.297352000
3 C2	0.000000000	0.000000000	0.067000000C.2	1 MOL	0.652199000
4 F1	0.000000000	−1.087000000	−0.699000000F	1 MOL	−0.213745000
5 F2	0.000000000	1.087000000	−0.699000000F	1 MOL	−0.213745000
6 H2	0.000000000	−0.938000000	1.924000000H	1 MOL	0.297352000

@<TRIPOS > BOND		
1	1	2 1
2	1	3 2
3	1	6 1
4	3	4 1
5	3	5 1

@<TRIPOS > SUBSTRUCTURE		
1	MOL	1
@<TRIPOS > COMMENT.		

Appendix D. R1132a Gromacs topology file

```
; Topology files based on OPLS/AA-L and AMBER03 customized for R1132(E) available on Gromacs
; Details are given in the paper:
; T. Imai, T. Kawahara, R. Nonaka, S. Tomassetti, T. Okumura, Y. Higashi, G. Di Nicola, C. Kondou
; "Surface Tension Measurement and Molecular Simulation for New Low Global Warming Potential
; Refrigerants R1132(E) and R1132a"
;Journal of Molecular Liquids
```

[defaults].

; nbfunc	comb-rule	gen-pairs	fudgeLJ	fudgeQQ
1	2	yes	0.5	0.5

[atomtypes].

;name		mass	q		sigma	epsiron
C_01	6	0.0	0.0	A	0.3620	0.41000
C_02	6	0.0	0.0	A	0.3520	0.38000
H_01	1	0.0	0.0	A	0.2450	0.06450
F_01	9	0.0	0.0	A	0.2900	0.22300

[moleculetype].

;name	nrexcl
MOL01	3

[atoms].

;nr	type	resi	res	atom	cgnr	charge	mass
1	C_01	1	MOL01	C	1	−0.819413	12.01100
2	H_01	1	MOL01	H	2	0.297352	1.00794
3	C_02	1	MOL01	C	3	0.652199	12.01100
4	F_01	1	MOL01	F	4	−0.213745	18.99840
5	F_01	1	MOL01	F	5	−0.213745	18.99840
6	H_01	1	MOL01	H	6	0.297352	1.00794

[bonds].

;ai	aj	funct	r	k
1	2	1	1.07932e-01	1.82281e+05
1	3	1	1.32268e-01	3.07586e+05
1	6	1	1.07932e-01	1.82281e+05
3	4	1	1.32957e-01	2.06755e+05
3	5	1	1.32957e-01	2.06755e+05

[pairs].

2	4	1
2	5	1
6	4	1
6	5	1

[angles].

;ai	aj	ak	funct	theta	cth
1	3	4	1	1.2519e+02	3.8814e+02
1	3	5	1	1.2519e+02	3.8814e+02
2	1	3	1	1.1966e+02	1.9907e+02
2	1	6	1	1.2068e+02	1.9507e+02
3	1	6	1	1.1966e+02	1.9907e+02
4	3	5	1	1.0963e+02	5.5513e+02

[dihedrals].

2	1	3	4	9	180.00	27.82360	2
2	1	3	5	9	180.00	27.82360	2
6	1	3	4	9	180.00	27.82360	2
6	1	3	5	9	180.00	27.82360	2
1	4	3	5	4	180.00	4.602400	2
6	1	2	3	4	180.00	4.602400	2

[system]
R1132a_CCSD_DGTZVP_RESP on 2023 Nov. 03 tuned by T. Imai
[molecules]
MOL01 3000

Appendix E. Measured saturation density for R1132(E)

The saturation density data of R1132(E) were obtained by visual observation of meniscal disappearance and reading the intersection of the saturation curve and isochore lines of *PvT* data. The apparatus and methods were identical to those described by Sakoda et al. [13]. The purity of the R1132(E) sample used in this measurement was 99.6 %. The uncertainties in the density and temperature measurements ($k = 2$) were estimated to be within 0.15 % and 5 mK, respectively.

Table A1
Saturation density data measured for R1132(E).

Meniscus		*PvT*	
Temperature (ITS-90) T [K]	Saturation density ρ [kg m^{-3}]	Temperature (ITS-90) T [K]	Saturation density ρ [kg m^{-3}]
338.597	193.6	312.54	86.4
343.682	244.9	333.71	161.5
345.688	270.5	337.95	714.3
348.160	319.1	307.23	899.3
348.472	342.3		
348.718	433.1		
348.720	446.0		
348.691	478.5		
347.183	564.4		
345.255	605.6		
329.863	766.8		

Appendix F. MD simulation results and benchmark tests

Table A.2 provides the numerical results of the MD simulations plotted in Figs. 5 through 7. A benchmark test of the MD simulation is also included below because the cutoff and simulation cell size in the calculation conditions can affect the results. Table A.3 lists the physical properties obtained by varying the cell size (and thus the number of molecules) and the cutoff.

The results for a cutoff of 1.5 nm at 160 K shown in the third row of Table A3 are also shown in Table A2 for the same conditions. In comparison, the surface tension differs by 1.5 mN m^{-1}, the saturation pressure by 0.065 kPa, the liquid density by 0.5 kg m^{-3}, and the vapor density by 0.18 kg m^{-3}. Fig. A.1 shows the time evolution in the obtained properties at 160 K, cutoff 1.5 nm, and number of molecules 2500, as listed in the third row of Table A.3. The mean value for the 4 to 6 ns period when equilibration is complete is plotted by the horizontal solid line, and the standard deviation is plotted by the dashed line. The effect of molecular initial configuration was comparable to or slightly larger than the standard deviation. However, the effect on saturated vapor density was about three times larger than the standard deviation.

The simulation with number of molecules increased from 2500 to 5000 in the simulation cell box size expanded from 6 nm square to 7.5 nm square (9 nm square only at 270 K) in the xy-plane parallel to the vapor–liquid interface, was performed at temperatures 160, 200, and 270 K for comparison. The differences were 1.17 mN m^{-1} in surface tension, 2.2 kPa in saturation pressure, 0.6 kg m^{-3} in liquid density, and 0.14 kg m^{-3} in vapor density. The former three values were approximately the time-variation; however, the saturated vapor was slightly more than twice the standard deviation.

Table A3 also shows the results of changing the cutoff at a temperature of 160 K, where the effect of the cutoff is more noticeable. Fig. A2 plots the obtained physical properties against different cutoff values on the horizontal axis. Assuming the Lennard-Jones size parameter for a molecule is 0.4 nm, a cutoff of 1.5 nm corresponds to 3.75 times this size, and a cutoff of 2.5 nm corresponds to 6.25 times this size. The liquid density stopped increasing and remained constant at a cutoff of 2.3 nm or higher. The liquid density calculated with a cutoff of 1.5 nm is 0.9934 times the plateau liquid density. A decrease in vapor density and saturation pressure appears somewhat moderate at cutoffs greater than 2.0 nm. However, the surface

tension increases monotonically up to 2.5 nm. The effect of the cutoff differs according to the physical properties. The effect of the cutoff on surface tension is particularly large, and the calculated surface tension does not agree with the measured values except for the cutoff of 1.5 nm.

Table A2
MD simulation data with a cutoff of 1.5 nm. (detailed simulation conditions are listed in Table 2).

Substance	Temp. [K]	Pressure [MPa]	Liquid density [kg m^{-3}]	Vapor density [kg m^{-3}]	Surface tension [mNm^{-1}]
R1132(E)	200	0.026	1214.1	1.28	23.67
	210	0.038	1190.2	2.21	21.04
	220	0.079	1165.5	3.62	19.26
	230	0.129	1140.0	5.65	17.70
	240	0.207	1113.7	8.48	15.63
	250	0.332	1086.3	12.33	14.10
	260	0.484	1057.6	17.45	12.20
	270	0.696	1027.4	24.16	10.39
	280	0.976	995.2	32.85	8.96
	290	1.31	960.7	44.10	7.53
	300	1.71	923.1	58.66	5.23
	310	2.32	881.2	77.77	4.63
	320	2.86	833.1	103.5	2.73
	330	3.68	774.4	139.9	1.87
R1132a	150	0.0019	1216.9	0.30	23.67
	160	0.0062	1191.0	0.52	22.72
	170	0.020	1165.0	1.04	19.92
	180	0.043	1139.2	2.18	17.49
	190	0.088	1109.1	4.01	16.27
	200	0.144	1081.4	5.72	14.06
	210	0.264	1052.8	10.46	12.63
	220	0.422	1022.7	15.64	10.77
	230	0.591	988.7	21.59	9.29
	240	0.886	951.0	32.96	7.73
	250	1.17	914.6	44.31	6.37
	260	1.67	873.6	67.40	4.33
	270	2.05	830.8	81.33	3.39

Table A3
Benchmark data of MD simulation to confirm the effects of cutoff and number of molecules for R1132a.

Temp. [K]	cutoff [nm]	#mole	Pressure [MPa]	Liquid density [kg m^{-3}]	Vapor density [kg m^{-3}]	Surface tension [mNm^{-1}]	Cell size [nm]
120	1.5	2500	N/A*	1290.0	N/A*	29.96	6.5 × 6.5 × 80
160	1.3	2500	0.0047	1187.3	0.71	20.42	6.0 × 6.0 × 80
160	1.5	2500	0.0071	1190.5	0.70	21.20	6.0 × 6.0 × 80
160	1.7	2500	0.0025	1193.2	0.62	22.37	6.0 × 6.0 × 80
160	2.0	2500	0.0051	1196.9	0.52	22.94	6.0 × 6.0 × 80
160	2.3	2500	0.0043	1198.9	0.56	24.11	6.0 × 6.0 × 80
160	2.5	2500	0.0020	1198.9	0.46	24.54	6.0 × 6.0 × 80
160	1.5	5000	0.0093	1191.1	0.84	22.37	7.5 × 7.5 × 75
200	1.7	2500	0.145	1083.5	7.13	15.62	6.0 × 6.0 × 60
200	2.0	2500	0.138	1090.8	5.99	15.07	6.0 × 6.0 × 60
200	1.5	5000	0.167	1080.5	6.75	14.84	7.5 × 7.5 × 75
270	1.5	2500	2.19	822.1	92.20	3.01	6.0 × 6.0 × 35
270	1.5	5000	2.10	825.6	84.60	3.48	9.0 × 9.0 × 40

*The number of molecules in the vapor phase is too small to calculate statistically averaged values.

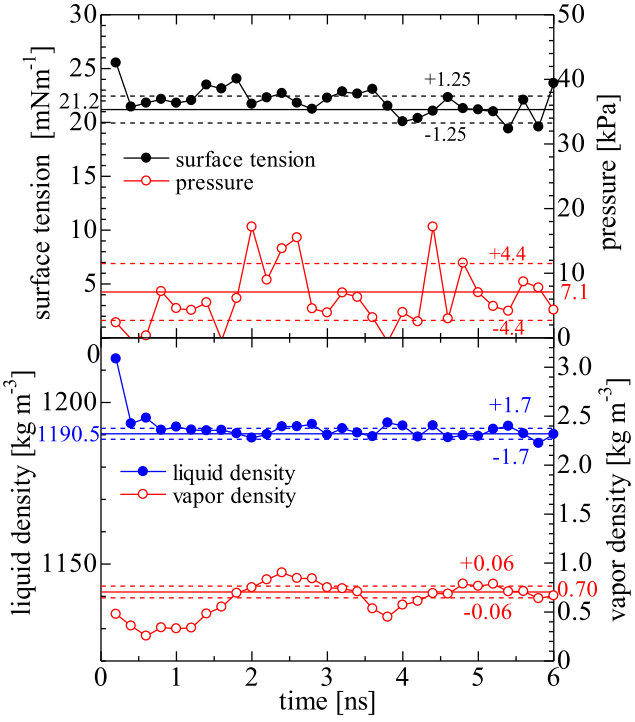

Fig. A1. Time variation in the average value of every 0.2 ns of the R1132a equilibration process at a temperature of 160 K calculated with a cutoff of 1.5 nm. The arithmetic mean of 4 to 6 ns is shown by the horizontal solid line. The horizontal dashed line shows the standard deviation of this time interval.

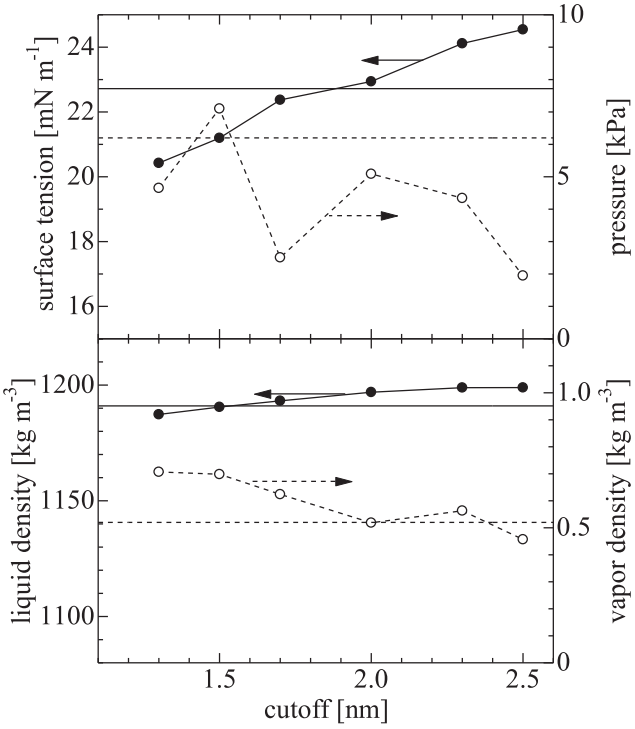

Fig. A2. Effect of cutoff variation on the obtained physical properties of R1132a at a temperature of 160 K. Symbols are the values shown in . Horizontal solid and dashed lines are calculated with a cutoff of 1.5 nm, shown in .

Appendix G. Supplementary data

Supplementary data to this article can be found online at https://doi.org/10.1016/j.molliq.2024.125262.

References

[1] M.D.P. Smith, C., Z.R.J. Nicholls, K. Armour, W. Collins, P. Forster, M. Meinshausen, The Earth's Energy Budget, Climate Feedbacks, and Climate Sensitivity Supplementary Material. In Climate Change 2021: The Physical Science Basis. Contribution of Working Group I to the Sixth Assessment Report of the Intergovernmental Panel on Climate Chan, 2021. DOI: 10.1017/9781009157896.009.

[2] W. Steffen, K. Richardson, J. Rockström, S.E. Cornell, I. Fetzer, E.M. Bennett, R. Biggs, S.R. Carpenter, W. de Vries, C.A. de Wit, C. Folke, D. Gerten, J. Heinke, G.M. Mace, L.M. Persson, V. Ramanathan, B. Reyers, S. Sörlin, Planetary boundaries: Guiding human development on a changing planet, Science (80-.). 347 (2015) 1259855. DOI: 10.1126/science.1259855.

[3] C. Xu, T.A. Kohler, T.M. Lenton, J.C. Svenning, M. Scheffer, Future of the human climate niche, Proc. Natl. Acad. Sci. USA 117 (2020), https://doi.org/10.1073/pnas.1910114117.

[4] P. Hawken, Drawdown: The most comprehensive plan ever proposed to reverse global warming, Penguin, 2017.

[5] M.O. McLinden, M.L. Huber, (R)Evolution of Refrigerants, J. Chem. Eng. Data. 65 (2020) 4176–4193, https://doi.org/10.1021/acs.jced.0c00338.

[6] ECHA(European Chemicals Agency), Per- and polyfluoroalkyl substances (PFAS), (2023). https://echa.europa.eu/hot-topics/perfluoroalkyl-chemicals-pfas#:~:text=The European Commission commits to,irreplaceable and essential to society.&text=The recast of the Drinking,µg%2Fl for all PFAS.

[7] U. Perera, K. Miyane, N. Sakoda, K. Thu, Y. Higashi, PvT Properties and Thermodynamic Property Correlations for the Low Global Warming Potential Hydrofluoroolefin Refrigerant R-1132a (1,1-Difluoroethene), Int. J. Thermophys. 44 (2023) 84, https://doi.org/10.1007/s10765-023-03184-4.

[8] N. Sakoda, U.A. Perera, K. Thu, Y. Higashi, Measurements of PvT properties, saturated densities, and critical parameters of R1132(E), Int. J. Refrig. 140 (2022) 166–171, https://doi.org/10.1016/j.ijrefrig.2022.05.012.

[9] S. Tomassetti, G. Di Nicola, C. Kondou, Triple point measurements for new low-global-warming-potential refrigerants: Hydro-fluoro-olefins, hydro-chloro-fluoro-olefins, and trifluoroiodomethane, Int. J. Refrig. 133 (2022) 172–180, https://doi.org/10.1016/j.ijrefrig.2021.10.008.

[10] G. Raabe, Molecular Dynamics Studies on Liquid-Phase Dynamics and Structures of Four Different Fluoropropenes and Their Binary Mixtures with R-32 and CO2, J. Phys. Chem. B. 118 (2014) 240–254, https://doi.org/10.1021/jp409408k.

[11] G. Raabe, Molecular Simulation Studies on the Vapor-Liquid Equilibria of the cis- and trans-HCFO-1233zd and the cis-and trans-HFO-1336mzz, J. Chem. Eng. Data. 60 (2015) 2412–2419, https://doi.org/10.1021/acs.jced.5b00286.

[12] G. Raabe, E.J. Maginn, A force field for 3,3,3-fluoro-1-propenes, including HFO-1234yf, J. Phys. Chem. B. 114 (2010) 10133–10142, https://doi.org/10.1021/jp102534z.

[13] G. Raabe, Molecular simulation studies on refrigerants past – present – future, Fluid Phase Equilib. 485 (2019) 190–198, https://doi.org/10.1016/j.fluid.2018.12.022.

[14] G. Raabe, M.G. Hopkins, C.C. Sampson, P.L. Stanwix, E.F. May, Dielectric properties of binary hydrofluoroolefin refrigerant mixtures: Comparisons of new experimental data with molecular dynamics simulations, J. Chem. Thermodyn. 142 (2020) 105985, https://doi.org/10.1016/j.jct.2019.105985.

[15] J. Algaba, M. Cartes, A. Mejía, J.M. Míguez, F.J. Blas, Phase Equilibria and Interfacial Properties of the Tetrahydrofuran + Methane Binary Mixture from Experiment and Computer Simulation, J. Phys. Chem. c. 123 (2019) 20960–20970, https://doi.org/10.1021/acs.jpcc.9b05412.

[16] S. Stephan, S. Becker, K. Langenbach, H. Hasse, Vapor-liquid interfacial properties of the system cyclohexane + CO2: Experiments, molecular simulation and density gradient theory, Fluid Phase Equilib. 518 (2020) 112583, https://doi.org/10.1016/j.fluid.2020.112583.

[17] S. Stephan, F. Fleckenstein, H. Hasse, Vapor-Liquid Interfacial Properties of the Systems (Toluene + CO2) and (Toluene + N2): Experiments, Molecular Simulation, and Density Gradient Theory, J. Chem. Eng. Data. 69 (2024) 590–607, https://doi.org/10.1021/acs.jced.3c00338.

[18] A. Mejia, M. Cartes, H. Segura, E.A. Müller, Use of equations of state and coarse grained simulations to complement experiments: Describing the interfacial properties of carbon dioxide + decane and carbon dioxide + eicosane mixtures, J. Chem. Eng. Data. 59 (2014) 2928–2941, https://doi.org/10.1021/je5000764.

[19] ASHRAE, ANSI/ASHRAE Standard 34-2022, Designation and Safety Classification of Refrigerants, 2022. https://www.ashrae.org/technical-resources/standards-and-guidelines/ashrae-refrigerant-designations.

[20] U.A. Perera, N. Sakoda, T. Miyazaki, K. Thu, Y. Higashi, Measurements of saturation pressures for the novel refrigerant R1132(E), Int. J. Refrig. 135 (2022) 148–153, https://doi.org/10.1016/j.ijrefrig.2021.12.014.

[21] K.S. Pitzer, The Volumetric and Thermodynamic Properties of Fluids. I. Theoretical Basis and Virial Coefficients 1, J. Am. Chem. Soc. 77 (1955) 3427–3433, https://doi.org/10.1021/ja01618a001.

[22] Y. Duan, C. Wu, S. Chowdhury, M.C. Lee, G. Xiong, W. Zhang, R. Yang, P. Cieplak, R. Luo, T. Lee, J. Caldwell, J. Wang, P. Kollman, A Point-Charge Force Field for Molecular Mechanics Simulations of Proteins Based on Condensed-Phase Quantum Mechanical Calculations, J. Comput. Chem. 24 (2003) 1999–2012, https://doi.org/10.1002/jcc.10349.

[23] C.I. Bayly, P. Cieplak, W.D. Cornell, P.A. Kollman, A well-behaved electrostatic potential based method using charge restraints for deriving atomic charges: The RESP model, J. Phys. Chem. 97 (1993) 10269–10280, https://doi.org/10.1021/j100142a004.

[24] W.L. Jorgensen, D.S. Maxwell, J. Tirado-Rives, Development and testing of the OPLS all-atom force field on conformational energetics and properties of organic liquids, J. Am. Chem. Soc. 118 (1996) 11225–11236, https://doi.org/10.1021/ja9621760.

[25] G. Raabe, Molecular Simulation Studies on Thermophysical Properties, Springer Singapore, Singapore (2017), https://doi.org/10.1007/978-981-10-3545-6.

[26] G. Raabe, Parameterization Approach for a Systematic Extension of the Hydrofluoroolefin Force Field to Fluorinated Butenes and Hydrochlorofluoroolefin Compounds, J. Chem. Eng. Data. 65 (2020) 1234–1242, https://doi.org/10.1021/acs.jced.9b00588.

[27] M.J. Frisch, G.W. Trucks, H.B. Schlegel, G.E. Scuseria, M.A. Robb, J.R. Cheeseman, G. Scalmani, V. Barone, G.A. Petersson, H. Nakatsuji, X. Li, M. Caricato, A. V. Marenich, J. Bloino, B.G. Janesko, R. Gomperts, B. Mennucci, H.P. Hratchian, J. V. Ortiz, A.F. Izmaylov, J.L. Sonnenberg, D. Williams-Young, F. Ding, F. Lipparini, F. Egidi, J. Goings, B. Peng, A. Petrone, T. Henderson, D. Ranasinghe, V. G. Zakrzewski, J. Gao, N. Rega, G. Zheng, W. Liang, M. Hada, M. Ehara, K. Toyota, R. Fukuda, J. Hasegawa, M. Ishida, T. Nakajima, Y. Honda, O. Kitao, H. Nakai, T. Vreven, K. Throssell, J.A. Montgomery Jr., J.E. Peralta, F. Ogliaro, M. J. Bearpark, J.J. Heyd, E.N. Brothers, K.N. Kudin, V.N. Staroverov, T.A. Keith, R. Kobayashi, J. Normand, K. Raghavachari, A.P. Rendell, J.C. Burant, S.S. Iyengar, J. Tomasi, M. Cossi, J.M. Millam, M. Klene, C. Adamo, R. Cammi, J.W. Ochterski, R.L. Martin, K. Morokuma, O. Farkas, J.B. Foresman, D.J. Fox, Gaussian16 {r} evision {C}.01 (2016).

[28] J. Wang, W. Wang, P.A. Kollman, D.A. Case, Automatic atom type and bond type perception in molecular mechanical calculations, J. Mol. Graph. Model. 25 (2006) 247–260, https://doi.org/10.1016/j.jmgm.2005.12.005.

[29] A.W. Sousa Da Silva, W.F. Vranken, ACPYPE - AnteChamber PYthon Parser interfacE, BMC Res. Notes. 5 (2012) 1–8, https://doi.org/10.1186/1756-0500-5-367.

[30] K. Vanommeslaeghe, E. Hatcher, C. Acharya, S. Kundu, S. Zhong, J. Shim, E. Darian, O. Guvench, P. Lopes, I. Vorobyov, A.D. Mackerell, CHARMM general force field: A force field for drug-like molecules compatible with the CHARMM all-atom additive biological force fields, J. Comput. Chem. 31 (2010) 671–690, https://doi.org/10.1002/jcc.21367.

[31] N.A.S. Reinier L. C. Akkermans, S.H. Robertson, COMPASS III: automated fitting workflows and extension to ionic liquids, Mol. Simul. 47 (2021) 540–551. DOI: 10.1080/08927022.2020.1808215.

[32] F. Ritschl, M. Fait, K. Fiedler, J.E.H. Köhler, B. Kubias, M. Meisel, An Extension of the Consistent Valence Force Field (CVFF) with the Aim to Simulate the Structures of Vanadium Phosphorus Oxides and the Adsorption of n-Butane and of 1-Butene on their Crystal Planes, Zeitschrift Für Anorg. Und Allg. Chemie. 628 (2002) 1385, https://doi.org/10.1002/1521-3749(200206)628:6<1385::AID-ZAAC1385>3.0.CO;2-1.

[33] K. Sasaki, T. Yamashita, Modification and Validation of the DREIDING Force Field for Molecular Liquid Simulations (DREIDING-UT), J. Chem. Inf. Model. 61 (2021) 1172–1179, https://doi.org/10.1021/acs.jcim.0c01169.

[34] H. Cao, X. Cao, J. Chen, X. Zhao, G. Ding, D. Guo, Y. Liu, H. Li, J. Bian, Molecular dynamics simulation of the transport properties and condensation mechanism of carbon dioxide, J. Nat. Gas Sci. Eng. 105 (2022) 104692, https://doi.org/10.1016/j.jngse.2022.104692.

[35] E.M. Blokhuis, D. Bedeaux, C.D. Holcomb, J.A. Zollweg, Tail corrections to the surface tension of a Lennard-Jones liquid-vapour interface, Mol. Phys. 85 (1995) 665–669, https://doi.org/10.1080/00268979500101371.

[36] M. Mecke, J. Winkelmann, J. Fischer, Molecular dynamics simulation of the liquid-vapor interface: The Lennard-Jones fluid, J. Chem. Phys. 107 (1997) 9264–9270, https://doi.org/10.1063/1.475217.

[37] A. Trokhymchuk, J. Alejandre, Computer simulations of liquid/vapor interface in Lennard-Jones fluids: Some questions and answers, J. Chem. Phys. 111 (1999) 8510–8523, https://doi.org/10.1063/1.480192.

[38] E.A. Muller, Å. Ervik, A. Mejía, A Guide to Computing Interfacial Properties of Fluids from Molecular Simulations [Article v1.0], Living J. Comput. Mol. Sci. 2 (2020), https://doi.org/10.33011/livecoms.2.1.21385.

[39] G.D. Purvis, R.J. Bartlett, A full coupled-cluster singles and doubles model: The inclusion of disconnected triples, J. Chem. Phys. 76 (1982) 1910–1918, https://doi.org/10.1063/1.443164.

[40] N. Godbout, D.R. Salahub, J. Andzelm, E. Wimmer, Optimization of Gaussian-type basis sets for local spin density functional calculations. Part I. Boron through neon, optimization technique and validation, Can. J. Chem. 70 (1992) 560–571, https://doi.org/10.1139/v92-079.

[41] C. Sosa, J. Andzelm, B.C. Elkin, E. Wimmer, K.D. Dobbs, D.A. Dixon, A local density functional study of the structure and vibrational frequencies of molecular transition-metal compounds, J. Phys. Chem. 96 (1992) 6630–6636, https://doi.org/10.1021/j100195a022.

[42] M.J. Abraham, T. Murtola, R. Schulz, S. Páll, J.C. Smith, B. Hess, E. Lindah, Gromacs: High performance molecular simulations through multi-level parallelism from laptops to supercomputers, SoftwareX. 1–2 (2015) 19–25, https://doi.org/10.1016/j.softx.2015.06.001.

[43] H.J.C. Berendsen, D. van der Spoel, R. van Drunen, GROMACS: A message-passing parallel molecular dynamics implementation, Comput. Phys. Commun. 91 (1995) 43–56, https://doi.org/10.1016/0010-4655(95)00042-E.

[44] M.A. Cuendet, W.F. Van Gunsteren, On the calculation of velocity-dependent properties in molecular dynamics simulations using the leapfrog integration algorithm, J. Chem. Phys. 127 (2007) 1–8, https://doi.org/10.1063/1.2779878.

[45] T. Darden, D. York, L. Pedersen, Particle mesh Ewald: An N ·log(N) method for Ewald sums in large systems, J. Chem. Phys. 98 (1993) 10089–10092, https://doi.org/10.1063/1.464397.

[46] S. Nosé, A unified formulation of the constant temperature molecular dynamics methods, J. Chem. Phys. 81 (1984) 511–519, https://doi.org/10.1063/1.447334.

[47] W.G. Hoover, Canonical dynamics: Equilibrium phase-space distributions, Phys. Rev. A. 31 (1985) 1695–1697, https://doi.org/10.1103/PhysRevA.31.1695.
[48] B. Hess, H. Bekker, H.J.C. Berendsen, J.G.E.M. Fraaije, LINCS: A linear constraint solver for molecular simulations, J. Comput. Chem. 18 (1997) 1463–1472, https://doi.org/10.1002/(SICI)1096-987X(199709)18:12<1463::AID-JCC4>3.0.CO;2-H.
[49] L. Rayleigh, On the theory of the capillary tube, Proc. R. Soc. A Math. Phys. Eng. Sci. 92 (1916) 184–195, https://doi.org/10.1098/rspa.1916.0004.
[50] M. Okada, Study on Saturated Liquid Density and Surface Tension of CFC Refrigerants, Keio University, 1984. Doctoral Thesis,.
[51] C. Kondou, Y. Higashi, S. Iwasaki, Surface Tension and Parachor Measurement of Low-Global Warming Potential Working Fluid cis-1-Chloro-2,3,3,3-tetrafluoropropene (R1224yd(Z)), J. Chem. Eng. Data. 64 (2019) 5462–5468, https://doi.org/10.1021/acs.jced.9b00613.
[52] R. Evans, J.R. Henderson, D.C. Hoyle, A.O. Parry, Z.A. Sabeur, Asymptotic decay of liquid structure: oscillatory liquid-vapour density profiles and the Fisher-Widom line, Mol. Phys. 80 (1993) 755–775, https://doi.org/10.1080/00268979300102621.
[53] S. Stephan, J. Liu, K. Langenbach, W.G. Chapman, H. Hasse, Vapor−Liquid Interface of the Lennard-Jones Truncated and Shifted Fluid: Comparison of Molecular Simulation, Density Gradient Theory, and Density Functional Theory, J. Phys. Chem. c. 122 (2018) 24705–24715, https://doi.org/10.1021/acs.jpcc.8b06332.
[54] J. Gross, G. Sadowski, Perturbed-Chain SAFT: An Equation of State Based on a Perturbation Theory for Chain Molecules, Ind. Eng. Chem. Res. 40 (2001) 1244–1260, https://doi.org/10.1021/ie0003887.
[55] I. Anoune, Z. Mimoune, H. Madani, A. Merzougui, New modified PC-SAFT pure component parameters for accurate VLE and critical phenomena description, Fluid Phase Equilib. 532 (2021) 112916, https://doi.org/10.1016/j.fluid.2020.112916.
[56] W. Pentermann, W. Wagner, New pressure-density-temperature measurements and new rational equations for the saturated liquid and vapour densities of oxygen, J. Chem. Thermodyn. 10 (1978) 1161–1172, https://doi.org/10.1016/0021-9614(78)90033-2.
[57] D. Peng, D.B. Robinson, A New Two-Constant Equation of State, Ind. Eng. Chem. Fundam. 15 (1976) 59–64, https://doi.org/10.1021/i160057a011.
[58] A.M. Abudour, S.A. Mohammad, R.L. Robinson, K.A.M. Gasem, Volume-translated Peng-Robinson equation of state for saturated and single-phase liquid densities, Fluid Phase Equilib. 335 (2012) 74–87, https://doi.org/10.1016/j.fluid.2012.08.013.
[59] R.W. Hankinson, G.H. Thomson, A new correlation for saturated densities of liquids and their mixtures, AIChE J. 25 (1979) 653–663, https://doi.org/10.1002/aic.690250412.
[60] K. Tanaka, J. Ishikawa, K.K. Kontomaris, Thermodynamic properties of HFO-1336mzz(E) (trans-1,1,1,4,4,4-hexafluoro-2-butene) at saturation conditions, Int. J. Refrig. 82 (2017) 283–287, https://doi.org/10.1016/j.ijrefrig.2017.06.012.
[61] Y. Kayukawa, Y. Fujita, Y. Kano, Theoretical performance of cryogenic-temperature applications using R23 alternative low-GWP refrigerant, R1132a (1,1-difluoroethene), 2nd IIR Conf, Hfos Low GWP Blends. (2021) 237–243, https://doi.org/10.18462/iir.HFO.2021.1050.
[62] K. Thu, U.A. Perera, K. Miyane, N. Sakoda, Y. Higashi, Vapour Pressure Measurements and Correlations for 1,1-Difluoroethene (R-1132a) at 240–296 K using a Newly Developed Isochoric Apparatus, Int. J. Thermophys. 44 (2023) 61, https://doi.org/10.1007/s10765-023-03167-5.
[63] Y. Higashi, Measurement of the Critical Parameters for low GWP Refrigerant R1132a, in: 2022 JSRAE Annu. Conf. Sep. 7-9, Okayama, 2022: pp. 1–6.
[64] S. Tomassetti, G. Di Nicola, Saturated pressure and vapor-phase pvT measurements of 1,1-difluoroethene (R1132a), Fluid Phase Equilib. 533 (2021) 112939, https://doi.org/10.1016/j.fluid.2021.112939.
[65] J. Otto, W. Thomas, Die thermischen zustandsgrössen von 1,1-difluoräthylen, Int. J. Heat Mass Transf. 7 (1964) 41–47, https://doi.org/10.1016/0017-9310(64)90022-5.
[66] G. Di Nicola, M. Moglie, A generalized equation for the surface tension of refrigerants, Int. J. Refrig. 34 (2011) 1098–1108, https://doi.org/10.1016/j.ijrefrig.2011.02.008.
[67] G. Di Nicola, C. Di Nicola, M. Moglie, A New Surface Tension Equation for Refrigerants, Int. J. Thermophys. 34 (2013) 2243–2260, https://doi.org/10.1007/s10765-011-0991-1.
[68] G. Di Nicola, G. Coccia, M. Pierantozzi, S. Tomassetti, Equations for the surface tension of low GWP halogenated alkene refrigerants and their blends, Int. J. Refrig. 86 (2018) 410–421, https://doi.org/10.1016/j.ijrefrig.2017.11.023.
[69] C. Miqueu, D. Broseta, J. Satherley, B. Mendiboure, J. Lachaise, A. Graciaa, An extended scaled equation for the temperature dependence of the surface tension of pure compounds inferred from an analysis of experimental data, Fluid Phase Equilib. 172 (2000) 169–182, https://doi.org/10.1016/S0378-3812(00)00384-8.
[70] D.B. Macleod, On a relation between surface tension and density, Trans. Faraday Soc. 19 (1923) 38, https://doi.org/10.1039/tf9231900038.
[71] S. Sugden, The Parachor and Molecular Volume, Nature. 125 (1930) 778–779, https://doi.org/10.1038/125778a0.
[72] R.H. Fowler, A tentative statistical theory of Macleod's equation for surface tension, and the parachor, Proc. r. Soc. London. Ser. A - Math. Phys. Sci. 159 (1937) 229–246, https://doi.org/10.1098/rspa.1937.0069.
[73] M.E. Boudh-Hir, G.A. Mansoori, Statistical mechanics basis of Macleod's formula, J. Phys. Chem. 94 (1990) 8362–8364, https://doi.org/10.1021/j100384a068.
[74] Y. Garrabos, F. Palencia, C. Lecoutre, D. Broseta, B. Le Neindre, Master crossover behavior of parachor correlations for one-component fluids, Phys. Rev. E - Stat. Nonlinear, Soft Matter Phys. 76 (2007) 1–24, https://doi.org/10.1103/PhysRevE.76.061109.
[75] V.P. Zhelezny, Y.V. Semenyuk, S.N. Ancherbak, N.V. Emel'yanenko, The temperature dependence of parachor, Russ. J. Phys. Chem. a. 83 (2009) 182–186, https://doi.org/10.1134/S0036024409020071.
[76] W. Wilding, R.L. Rowley, J.L. Oscarson, DIPPR® Project 801 evaluated process design data, Fluid Phase Equilib. (1998) 413–420.
[77] D.F. Ilten, DETHERM: thermophysical property data for the optimization of heat-transfer equipment, J. Chem. Inf. Comput. Sci. (1991) 160–167.